Atmos. Chem. Phys. Discuss., https://doi.org/10.5194/acp-2018-1090
Manuscript under review for journal Atmos. Chem. Phys.
Discussion started: 6 November 2018

Estimations of Global Shortwave Direct Aerosol Radiative Effects Above Opaque Water Clouds Using a Combination of A-Train Satellite Sensors

Meloë S. Kacenelenbogen [1]
Mark A. Vaughan [2]
Jens Redemann [3]
Stuart A. Young[4]
Zhaoyan Liu [2,4]
Yongxiang Hu[2]
Ali H. Omar [2]
Samuel LeBlanc [1],
Yohei Shinozuka [1],
John Livingston [1],
Qin Zhang [1],
Kathleen A. Powell [2]

[1]Bay Area Environmental Research Institute, Sonoma, CA, USA
[2]NASA Langley Research Center, Hampton, VA, USA
[3]University of Oklahoma, 120 David L. Boren Blvd., Suite 5900, Norman, OK
[4]Science Systems and Applications, Inc., Hampton, Virginia, USA

Correspondence to: Meloë S. Kacenelenbogen (meloe.s.kacenelenbogen@nasa.gov)

Abstract

All-sky Direct Aerosol Radiative Effects (DARE) play a significant yet still uncertain role in climate. This is partly due to poorly quantified radiative properties of Aerosol Above Clouds (AAC). We compute global estimates of short-wave top-of-atmosphere DARE over Opaque Water Clouds (OWC), $DARE_{OWC}$, using observation-based aerosol and cloud radiative properties from a combination of A-Train satellite sensors and a radiative transfer model. There are three major differences between our $DARE_{OWC}$ calculations and previous studies: (1) we use the Depolarization Ratio method (DR) on CALIOP (Cloud Aerosol LIdar with Orthogonal Polarization) Level 1 measurements to compute the AAC frequencies of occurrence and the AAC Aerosol Optical Depths (AOD), thus introducing fewer uncertainties compared to using the CALIOP standard product; (2) we apply our calculations globally, instead of focusing exclusively on regional AAC "hotspots" such as the southeast Atlantic; and (3) instead of the traditional look-up table approach, we use a combination of satellite-based sensors to obtain AAC intensive radiative properties. Our results agree with previous findings on the dominant locations of AAC (South and North East Pacific, Tropical and South East Atlantic, northern Indian Ocean and North West Pacific), the season of maximum occurrence, aerosol optical depths (a majority in the 0.01-0.02 range and that can exceed 0.2 at 532 nm) and aerosol extinction-to-backscatter ratios (a majority in the 40-50 sr range at 532 nm which is typical of dust aerosols) over the globe. We find positive averages of global seasonal $DARE_{OWC}$ between 0.13 and 0.26 $W \cdot m^{-2}$ (i.e., a warming effect on climate). Regional seasonal $DARE_{OWC}$ values range from -0.06 $W \cdot m^{-2}$ in the Indian Ocean, offshore from western Australia (in March-April-May) to 2.87 $W \cdot m^{-2}$ in the South East Atlantic (in September-

October-November). High positive values are usually paired with high aerosol optical depths (>0.1) and low single scattering albedos (<0.94), representative of, e.g., biomass burning aerosols. Because we use different spatial domains, temporal periods, satellite sensors, detection methods, and/or associated uncertainties, the $DARE_{OWC}$ estimates in this study are not directly comparable to previous peer-reviewed results. Despite these differences, we emphasize that the $DARE_{OWC}$ estimates derived in this study are generally higher than previously reported. The primary reasons for our higher estimates are (i) the possible underestimate of the number of dust-dominated AAC cases in our study; (ii) our use of Level 1 CALIOP products (instead of CALIOP Level 2 products in previous studies) for the detection and quantification of AAC aerosol optical depths, which leads to larger estimates of AOD above OWC; and (iii) our use of gridded 4ºx5º seasonal means of aerosol and cloud properties in our $DARE_{OWC}$ calculations instead of simultaneously derived aerosol and cloud properties from a combination of A-Train satellite sensors. Each of these areas is explored in depth with detailed discussions that explain both rationale for our specific approach and the subsequent ramifications for our DARE calculations.

Atmos. Chem. Phys. Discuss., https://doi.org/10.5194/acp-2018-1090
Manuscript under review for journal Atmos. Chem. Phys.
Discussion started: 6 November 2018

ACRONYMS

AAC	Aerosol-Above-Clouds
AAOD	Absorption Aerosol Optical Depth
AOD	Aerosol Optical Depth
$\tau^{DR}{}_{AAC}$	Aerosol Optical Depth above clouds using the DR method
AeroCom	Aerosol Comparisons between Observations and Models
AERONET	AErosol RObotic NETwork
AMSR-E	Advanced Microwave Scanning Radiometer - Earth Observing System
ARCTAS	Arctic Research of the Composition of the Troposphere from Aircraft and Satellites
ASR	integrated Attenuated Scattering Ratio
BRDF	Bidirectional Reflectance Distribution Function
CAC	Clear Air above Cloud
CALIOP	Cloud Aerosol LIdar with Orthogonal Polarization
CALIPSO	Cloud-Aerosol Lidar and Infrared Pathfinder Satellite Observations
CERES	Clouds and the Earth's Radiant Energy System
CF	Cloud Fraction
CloudSat	NASA Earth observation satellite
COD	Cloud Optical Depth

CR	Color Ratio technique
$DARE_{all\text{-}sky}$	Direct Aerosol Radiative Effect in all-sky conditions (cloudy and non-cloudy)
$DARE_{cloudy}$	Direct Aerosol Radiative Effect in cloudy conditions
$DARE_{non\text{-}cloudy}$	Direct Aerosol Radiative Effect in non-cloudy conditions (clear-skies)
$DARE_{OWC}$	Direct Aerosol Radiative Effect above opaque water clouds
DISORT	DIScrete ORdinate Radiative Transfer solvers
DR	Depolarization Ratio technique
δ^{OWC}	layer-integrated volume depolarization ratio
f_{AAC}	AAC frequency of occurrence
HSRL	High Spectral Resolution Lidar
IAB	Integrated Attenuated Backscatter
IBS	Integrated aerosol Backscatter
InWA	Indian ocean, offshore from West Australia
LUT	Look Up Table
LWP	Liquid Water Path
MBL	Marine Boundary Layer
MCD43GF	MODIS BRDF/Albedo/NBAR CMG Gap-Filled Products
MODIS	MODerate Imaging Spectroradiometer
η^{OWC}	layer effective multiple scattering factor

Atmos. Chem. Phys. Discuss., https://doi.org/10.5194/acp-2018-1090
Manuscript under review for journal Atmos. Chem. Phys.
Discussion started: 6 November 2018

NEAs	North East Asia
NEPa	North East Pacific ocean
NWPa	North West Pacific ocean
OMI	Ozone Monitoring Instrument
ORACLES	ObseRvations of Aerosols above CLouds and their intEractionS
OWC	Opaque Water Cloud
POLDER	Polarization and Directionality of Earth's Reflectances
PBL	Planetary Boundary Layer
R_e	Cloud droplet effective radius
RT	Radiative Transfer scheme
SAA	South Atlantic Anomaly
S_a	Aerosol extinction-to-backscatter (lidar) ratio
S_{AAC}	Aerosol extinction-to-backscatter (lidar) ratio above clouds
S_c	Cloud extinction-to-backscatter (lidar) ratio
SCIAMACHY	Scanning Imaging Absorption Spectrometer for Atmospheric Cartography
SEAs	South East Asia
SEAt	South East Atlantic ocean
SEPa	South East Pacific ocean
SEVIRI	Spinning Enhanced Visible and InfraRed Imager
SNR	Signal-to-Noise Ratio

Atmos. Chem. Phys. Discuss., https://doi.org/10.5194/acp-2018-1090
Manuscript under review for journal Atmos. Chem. Phys.
Discussion started: 6 November 2018

SS	Single Scattering
SSA	Single Scattering Albedo
SW	Short Wave
TAt	Tropical Atlantic ocean
TOA	Top Of Atmosphere

Atmos. Chem. Phys. Discuss., https://doi.org/10.5194/acp-2018-1090
Manuscript under review for journal Atmos. Chem. Phys.
Discussion started: 6 November 2018

Atmospheric Chemistry and Physics Discussions

1. Introduction

The Direct Aerosol Radiative Effect (DARE) is defined as the change in the upwelling radiative flux ($F^{\uparrow}$) at the top of the atmosphere (TOA) due to aerosols. Measured values of DARE depend on the accuracy and the geometry of the observation(s), the concentrations of various atmospheric constituents (e.g., aerosols, clouds, and atmospheric gases) and their radiative properties, and the Earth's surface reflectance. All-sky DARE ($DARE_{all\text{-}sky}$) combines contributions from DARE under cloudy conditions ($DARE_{cloudy}$) and DARE under cloud-free conditions ($DARE_{non\text{-}cloudy}$):

$$DARE_{all\text{-}sky} = DARE_{cloudy} \times \text{Cloud Fraction} + DARE_{non\text{-}cloudy} \times (1 - \text{Cloud Fraction}) \qquad \text{Eq. (1)}$$

According to Yu et al., [2006], substantial progress has been made in the assessment of $DARE_{non\text{-}cloudy}$ using satellite and in situ data. Further evidence is provided in a companion to our study, Redemann et al. [2018], which use A-Train aerosol observations to constrain $DARE_{non\text{-}cloudy}$ and compares the results with AeroCom (Aerosol Comparisons between Observations and Models) results (see Appendix A for further details). However, traditional passive aerosol remote sensing techniques are limited only to clear-sky conditions and significant efforts are required to estimate $DARE_{cloudy}$. Moreover, simulations of $DARE_{cloudy}$ from various AeroCom models in Schulz et al. [2006] (see their figure 6) show large disparities. Our study focuses on Aerosol Above Cloud (AAC) scenes over the globe and subsequent estimates of $DARE_{cloudy}$ (i.e., the instantaneous short wave (SW) upwelling TOA reflected radiative fluxes due to clouds only minus SW upwelling TOA fluxes due to clouds with overlying aerosols). Let us note that, ideally, TOA $DARE_{cloudy}$ should include aerosols below, in-between and above clouds. Here we assume that TOA $DARE_{cloudy}$ is only caused by aerosols above clouds. Table 1 lists TOA SW

DARE$_{cloudy}$ results that use satellite observations in the literature, together with assumptions in their calculations. Compared to the peer-reviewed studies of Table 1, our study marks a departure on three accounts. First, most peer-reviewed DARE$_{cloudy}$ calculations focus primarily on the South East Atlantic (SEAt e.g., [Chand et al., 2009, Wilcox et al., 2012, Peters et al., 2011, De Graaf et al., 2012, 2014, Meyer et al., 2013, 2015, Peers et al., 2015, Feng and Christopher, 2015] in Table 1). Second, our results use a combination of A-Train satellite sensors (i.e., MODIS-OMI-CALIOP), instead of the Look-Up-Table (LUT) approach used in the other studies of Table 1, to obtain estimates of the intensive aerosol radiative properties above clouds. Third, the peer-reviewed global DARE$_{cloudy}$ calculations in Table 1 use standard products from the active satellite sensor Cloud Aerosol LIdar with Orthogonal Polarization (CALIOP) for either AAC Aerosol Optical Depth (AOD) and/or aerosol and cloud vertical distribution information in the atmosphere [Zhang et al., 2014, 2016, Matus et al., 2015, Oikawa et al., 2013]. In our case, we estimate DARE$_{cloudy}$ globally by using an alternate method applied to CALIOP Level 1 measurements [Hu et al., 2007b; Chand et al., 2008; Liu et al., 2015] to obtain AAC AOD and the AAC frequency of occurrence. In the sections below, we explain why we have used such a method, instead of other passive or active satellite sensor techniques.

Table 1: TOA SW DARE$_{cloudy}$ calculations that use satellite observations in the literature and specific assumptions in the calculations. See also the theoretical study by Chang and Christopher et al. [2017] (i.e. they impose fixed COD, Re, AOD, aerosol radiative properties, and aerosol / cloud vertical distribution) and the study by Costantino and Bréon et al. [2013] (their method uses MODIS-derived cloud microphysics that are not corrected for overlying aerosols). When not specified, the study uses the standard CALIOP data product; otherwise, it uses the DR (Depolarization Ratio) or CR (Color Ratio)

Atmos. Chem. Phys. Discuss., https://doi.org/10.5194/acp-2018-1090
Manuscript under review for journal Atmos. Chem. Phys.
Discussion started: 6 November 2018

Atmospheric Chemistry and Physics Discussions

technique on CALIOP measurements. $MODIS^A$ and $MODIS^T$ respectively denote the AQUA or TERRA platform. SEAt: South East Atlantic. LUT: Look Up Table. See acronyms for satellite sensors MODIS, CALIOP, CloudSat, POLDER, CERES and AMSR-E.

Reference	Domain	Satellite sensor(s) used for $DARE_{cloudy}$ calculations			
		Cloud properties (e.g. COD, albedo, fraction)	AOD	Aerosol radia-tive properties (e.g. SSA, g)	Vertical distribution of aerosol and cloud
Chand et al. [2009]	SEAt	$MODIS^T$	$CALIOP^{CR}$	Fixed value	Assumed constant
Wilcox [2012]	SEAt	$MODIS^A$, AMSR-E	CERES provides upwelling shortwave flux		
Peters et al. [2011]	Atlantic	$MODIS^A$, AMSR-E	CERES provides upwelling shortwave flux		
De Graaf et al. [2012, 2014]	SEAt	Direct determination of $DARE_{cloudy}$ by building LUT of cloud and aerosol-free reflectances			
Meyer et al. [2013]	SEAt	$MODIS^A$	CALIOP	LUT approach	CALIOP
Zhang et al. [2014, 2016]	Globe	$MODIS^A$, CALIOP (uses probability density function of CALIOP above-cloud AOD and underlying MODIS COD)		LUT approach	CALIOP
Meyer et al. [2015]	SEAt	$MODIS^A$ (simultaneous retrieval of above-cloud AOD, COD and R_e)		LUT approach	Assumed constant
Peers et al. [2015]	SEAt	POLDER (simultaneous retrieval of above-cloud aerosol OD, size and single scattering albedo, cloud optical depth and cloud top height)			
Feng and Christopher [2015]	SEAt	$MODIS^A$, CERES	CERES provides upwelling shortwave flux		

Atmos. Chem. Phys. Discuss., https://doi.org/10.5194/acp-2018-1090
Manuscript under review for journal Atmos. Chem. Phys.
Discussion started: 6 November 2018

Reference	Domain	Satellite sensor(s) used for DARE$_{cloudy}$ calculations			
		Cloud properties (e.g. COD, albedo, fraction)	AOD	Aerosol radiative properties (e.g. SSA, g)	Vertical distribution of aerosol and cloud
Matus et al. [2015]	Globe	CloudSat, MODIS^{A}, CALIOP	CALIOP	LUT approach	CloudSat, CALIOP
Oikawa et al. [2013]	Globe	CALIOP, MODIS^{A}	CALIOP	LUT approach	CALIOP
This study	Globe	MODIS^{A}	CALIOP^{DR}	MODIS^{A}, OMI, CALIOP	Assumed constant

Table 2 lists some passive (i.e., Spinning Enhanced Visible and InfraRed Imager, SEVIRI, Moderate Resolution Imaging Spectroradiometer, MODIS, Polarization and Directionality of Earth's Reflectances, POLDER, Ozone Monitoring Instrument, OMI or the Scanning Imaging Absorption Spectrometer for Atmospheric Chartography, SCIAMACHY) and active (i.e., CALIOP and CloudSat) satellite sensors that were used to detect and quantify the AAC AODs. Among the peer-reviewed studies of Table 2, those few that present DARE$_{cloudy}$ results (see Table 1) are denoted by a "+" sign in the first column.

Table 2: Studies that observe AAC using passive and active satellite sensors (i.e., from left to right, SEVIRI, POLDER, CloudSat, OMI, MODIS, SCIAMACHY, CALIOP; see acronyms). When using CALIOP, the authors either use the standard Level 2 products (Std), the Depolarization method (DR) [Hu et al., 2007b] or the color ratio method (CR) [Chand et al., 2008]. SEAt stands for SE Atlantic,

Atmos. Chem. Phys. Discuss., https://doi.org/10.5194/acp-2018-1090
Manuscript under review for journal Atmos. Chem. Phys.
Discussion started: 6 November 2018

Atmospheric Chemistry and Physics Discussions

SEAs for SE Asia, NEAs for NE Asia and TAt for Tropical Atlantic. The "+" sign in the first column denotes the presence of $DARE_{cloudy}$ calculations.

	Reference	Domain	Satellite sensor(s) used for aerosol-above-cloud detection						
			SEVIRI	POLDER	CloudS	OMI	MODIS	SCIAMA	CALIOP
1	Chang and Christopher [2016, 2017^{+}]	SEAt							
2	Waquet et al. [2013a]	Globe							
3	Waquet et al. [2009, 2013b]	SEAt, TAt							
4	Peers et al. [2015]$^{+}$	SEAt							
5	Jethva et al [2013, 2014]	SEAt, TAt							
6	Torres et al. [2012]	SEAt							
7	Peters et al. [2011]$^{+}$	Atlantic							
8	De Graaf et al. [2012, 2014]$^{+}$	SEAt							
9	Meyer et al. [2015]$^{+}$	SEAt							
10	Feng and Christopher [2015]$^{+}$	SEAt							
11	Sayer et al. [2016]	SEAt, SEAs							
12	Matus et al. [2015]$^{+}$	Globe							Std
13	Alfaro-Contreras et al. [2016]	Globe							Std
14	Alfaro-Contreras et al. [2014]	SEAt, SEAs							Std
15	Devasthale and Thomas [2011]	Globe							Std
16	Yu et al. [2012]	SEAt, TAt							Std
17	Wilcox [2012]$^{+}$	SEAt							Std
18	Meyer et al. [2013]$^{+}$	SEAt							Std
19	Zhang et al. [2014, 2016]$^{+}$	Globe							Std
20	Oikawa et al. [2013]$^{+}$	Globe							Std
21	Chung et al. [2016]	Globe							Std
22	Chand et al. [2008]	SEAt							CR, DR

	Reference	Domain	Satellite sensor(s) used for aerosol-above-cloud detection						
			SEVIRI	POLDER	CloudS	OMI	MODIS	SCIAMA	CALIOP
23	Chand et al. [2009][+]	SEAt							CR
24	Deaconu et al. [2017]	Globe							Std, DR
25	Liu et al. [2015]	SEAt, TAt							DR
26	This study[+]	Globe							DR

The brightening of clear patches near clouds [Wen et al., 2007] (i.e., "3-D cloud radiative effect" or "cloud adjacency effect") can introduce biases into the current passive satellite AAC retrieval techniques (i.e., lines 1-11 of Table 2). To minimize these biases, this study relies primarily on CALIOP observations [Winker et al., 2009]. CALIOP is a three-channel elastic backscatter lidar with a narrow field of view and a narrow source of illuminating radiation, which limits cloud adjacency effects and the subsequent cloud contamination of aerosol data products [Zhang et al., 2005; Wen et al., 2007; Várnai and Marshak, 2009]. CALIOP measures high-resolution (1/3 km in the horizontal and 30m in the vertical in low and middle troposphere) profiles of the attenuated backscatter from aerosols and clouds at visible (532 nm) and near-infrared (1064 nm) wavelengths along with polarized backscatter in the visible channel [Hunt et al., 2009]. These data are distributed as part of the Level 1 CALIOP products. The Level 2 products are derived from the Level 1 products using a succession of sophisticated retrieval algorithms [Winker et al., 2009]. The Level 2 processing is composed of a feature detection scheme [Vaughan et al., 2009], a module that classifies features according to layer type (i.e., cloud versus aerosol) [Liu et al., 2010] and subtype (i.e., aerosol species) [Omar et al., 2009], and, finally, an extinction retrieval algorithm [Young and Vaughan, 2009] that retrieves profiles of aerosol backscatter and extinction coefficients and the total column AOD based on modeled values of the extinction-to-backscatter ratio (also called lidar ratio and represented by the symbol S_a) inferred for each detected aerosol layer subtype.

A few studies use standard CALIOP Level 2 Aerosol and Cloud Layer products to determine AAC occurrence over the globe (see line 12-21 in Table 2). However, a study by Kacenelenbogen et al. [2014] demonstrates that the standard version 3 CALIOP aerosol products substantially underreport the occurrence frequency of AAC when aerosol optical depths are less than ~0.02, mostly because these tenuous aerosol layers have attenuated backscatter coefficients less than the CALIOP detection threshold. CALIOP's standard extinction (and optical depth) data products are only retrieved between the tops and bases of detected features, and these boundaries may significantly underestimate the full vertical extent of the layer (Kim et al., 2017; Thorsen et al., 2017; Toth et al., 2018). Furthermore, the Kacenelenbogen et al. [2014] study found essentially no correlation between AAC AOD results reported by the CALIOP and collocated NASA Langley airborne High Spectral Resolution Lidar (HSRL). A subsequent study by Liu et al. [2015] shows that the CALIOP Level 2 standard aerosol data products underestimate dust AAC AOD by ~26% over the Tropical Atlantic and smoke AAC AOD by ~39% over the SE Atlantic.

For these reasons, a few studies in Table 2 (see line 22-26) use alternate methods on Level 1 CALIOP products, such as the Color Ratio (CR) [Chand et al., 2008] or the Depolarization Ratio (DR) [Hu et al., 2007b; Liu et al., 2015] methods, instead of using the AOD reported in the CALIOP standard Level 2 products.

In this study, we use the DR method and a combination of CALIOP Level 1 and Level 2 data products to compute global estimates of the AAC frequency of occurrence (i.e., f_{AAC}), the AAC AOD (i.e., τ^{DR}_{AAC}) and the AAC extinction-to-backscatter ratios (i.e., S_{AAC}) (section 2.1). We then use CALIOP results of f_{AAC}, τ^{DR}_{AAC} and other A-Train satellite products to compute global $DARE_{cloudy}$ (section 2.2). Section 3 describes the geographical and seasonal distribution of global f_{AAC} (section 3.1), τ^{DR}_{AAC} and S_{AAC} (section 3.2) and $DARE_{cloudy}$ results (section 3.3). Section 4 revisits some of the limitations in the method and proposes ways to improve on these $DARE_{cloudy}$ calculations.

2. Method

2.1. AAC optical depth and extinction-to-backscatter

The DR method can also be called the "constrained opaque water cloud method" [Liu et al, 2015] as it uses Opaque Water Clouds (OWCs) as reflectivity targets. The OWCs in this study are selected using the five criteria listed in Table B2 of the appendix. Most importantly, (1) only one cloud can be detected within a 5 km (15 shot) along-track average (which means, for example, that marine stratus below thin cirrus are excluded). Furthermore, this one cloud must be (2) opaque (which means that low but transparent clouds such as the ones reported in Leahy et al. [2012] are excluded), (3) spatially uniform (i.e., detected at single-shot resolution within every laser pulse included in the 5 km averaging interval), (4) assigned a high confidence score by the CALIOP cloud-aerosol discrimination (CAD) algorithm and (5) identified as a high confidence water cloud by the CALIOP cloud phase identification algorithm.When there is aerosol above OWCs, the lidar backscatter signal received from the underlying water cloud is reduced in direct proportion to the two-way transmittance of the aerosol layer above.

Atmos. Chem. Phys. Discuss., https://doi.org/10.5194/acp-2018-1090
Manuscript under review for journal Atmos. Chem. Phys.
Discussion started: 6 November 2018

Atmospheric Chemistry and Physics
Open Access
Discussions

Based on Hu et al. [2007a, 2007b], Eq. (2) describes how we compute τ^{DR}_{AAC} using the DR method above OWCs.

$$\tau^{DR}_{AAC} = -0.5 \times \ln[IAB^{OWC}_{SS,AAC} / IAB^{OWC}_{SS,CAC}] \quad \text{Eq. (2)}$$

Here $IAB^{OWC}_{SS,AAC}$ is the single scattering value (subscript SS) of the layer-integrated attenuated backscatter (IAB) for an OWC underlying one or more aerosol layer(s) above the cloud. $IAB^{OWC}_{SS,CAC}$ is the single scattering value of the IAB for an OWC underlying Clear air Above Cloud (CAC). By CAC, we mean that there are no aerosols detected above the OWC. In this study, we consider τ^{DR}_{AAC} valid when positive. According to Eq. (2), this means that $IAB^{OWC}_{SS,AAC}$ needs to always be smaller in magnitude than $IAB^{OWC}_{SS,CAC}$ and τ^{DR}_{AAC} equals zero when $IAB^{OWC}_{SS,AAC}$ equals $IAB^{OWC}_{SS,CAC}$.

Section B of the appendix provides additional information about the application of Eq. (2) and the various steps needed to derive τ^{DR}_{AAC}. We list the selection criteria used to identify the OWC dataset in this study and describe the corrections required to obtain single-scattering estimates of IAB from measurements that contain substantial contributions from multiple scattering (B1). We also describe the technique used for distinguishing between CAC and AAC conditions (B2), and illustrate our derivation of an empirical parameterization of $IAB^{OWC}_{SS,CAC}$ as a global function of latitude and longitude (B3).

As reported in Table 2, the CALIOP DR method was used to study the African dust transport pathway over the Tropical Atlantic [Liu et al., 2015] and the African smoke transport pathway over the South East Atlantic [Liu et al., 2015; Chand et al., 2008, 2009]. More recently, the CALIOP DR method was also used by Deaconu et al. [2017] to assess POLDER AAC AOD values [Waquet et al., 2009, 2013b and Peers et al., 2015] over the globe. In this study, we extend the previous regional studies of [Liu et

Atmos. Chem. Phys. Discuss., https://doi.org/10.5194/acp-2018-1090
Manuscript under review for journal Atmos. Chem. Phys.
Discussion started: 6 November 2018

al., 2015 and Chand et al., 2008, 2009] to derive global CALIOP-based AAC AOD estimates. S_{AAC} values are then computed by solving Eq. (15) of Fernald et al. [1972], constrained by valid (i.e., positive) $\tau^{DR}{}_{AAC}$ and using the GEOS-5 molecular and ozone number density values and the CALIOP Level 1 attenuated backscatter profiles (see step S5 in Table B1). Let us note that, in our study, the ability to retrieve CALIOP S_{AAC} has no bearing on the accuracy of our CALIOP $\tau^{DR}{}_{AAC}$ retrievals. The accuracy of $\tau^{DR}{}_{AAC}$ depends on measurements of targets of very high signal-to-noise ratio (SNR) such as OWCs in clear skies and OWCs underlying aerosols layers. On the other hand, many S_{AAC} retrievals depend on very low SNR measurements obtained from the weakly scattering and vertically diffuse aerosol layers above OWCs.

2.2. AAC Direct Aerosol Radiative Effects

Having first retrieved global values of $\tau^{DR}{}_{AAC}$ from the CALIOP measurements, we then compute global estimates of $DARE_{cloudy}$ using DISORT (DIScrete ORdinate Radiative Transfer; Stamnes et al., 1988, Buras et al., 2011), a six-stream plane-parallel radiative transfer model with molecular absorption characterized by a correlated-k scheme [Fu and Liou, 1992] that is embedded within the LibRadtran Radiative Transfer (RT) package [Emde et al., 2016]. Hereafter, our seasonally and spatially gridded (4º x 5º) averaged shortwave (SW) (250 nm to 5600 nm) global TOA $DARE_{cloudy}$ results will be called $DARE_{OWC}$, as they pertain to a specific category of clouds (i.e., OWCs) defined according to the CALIOP data selection criteria set forth in Table B2. We list the following input parameters to DISORT in order to derive estimates of $DARE_{OWC}$:

(1) **Atmospheric profiles** of pressure, temperature, air density, ozone, water vapor, CO_2, and NO_2 use standard US atmosphere profiles [Anderson et al., 1986].

(2) **Aerosol intensive radiative properties** (i.e. properties that depend solely on aerosol species, and are unrelated to the aerosol amount) are informed by seasonal maps (4° x 5°, daytime in 2007) of combined MODIS-OMI-CALIOP (MOC) retrieved median spectral extinction coefficients, single scattering albedos and asymmetry parameters at 30 different wavelengths. As an example, Figure A1 in the appendix shows the seasonal maps of MOC SSA at 546.3 nm that were used in the calculation of $DARE_{OWC}$. These MOC retrievals, described in section A of the appendix, are at the basis of a companion study [Redemann et al., 2018]. Let us note that we only use the shape of the MOC extinction coefficient spectra and not its actual magnitude; the MOC spectral extinction coefficient spectra is normalized to the seasonal 2008-2012 average value of either $\tau^{DR}{}_{AAC}$ or $\tau^{DR}{}_{AAC}$ x f_{AAC} within each grid cell. Our method assumes similar aerosol radiative properties above clouds and in near-by clear-sky regions.

(3) **Aerosol extensive radiative properties** (i.e., properties that depend on the aerosol amount present in the atmosphere) are informed by seasonal maps (4° x 5°, nighttime from 2008 to 2012) of either CALIOP $\tau^{DR}{}_{AAC}$ (see Eq. 2) or CALIOP $\tau^{DR}{}_{AAC}$ x $f_{AAC.}$ We chose to use nighttime CALIOP $\tau^{DR}{}_{AAC}$ or $\tau^{DR}{}_{AAC}$ x f_{AAC} results in the estimation of $DARE_{OWC}$ because, at nighttime, the CALIOP signal-to-noise-ratio (SNR) is not affected by ambient solar background and leads to a more accurate measurement of the aerosol signal (compared to daytime). By doing this, we implicitly chose a better accuracy in the aerosol extensive radiative properties over a temporal overlap between aerosol extensive (nighttime) and intensive (daytime) radiative properties.

(4) **Cloud albedos** are computed from cloud droplet effective radius (R_e) and Cloud Optical Depth (COD) information inferred from MODIS averaged monthly 1°x1° grids (i.e. liquid water cloud products of MYD08_M3: "Cloud Effective Radius Liquid Mean Mean" and "Cloud Optical Thickness Liquid Mean Mean" [Platnick et al. 2015]) from 2008 to 2012 (see Equations 1-9 of Peng et al. [2002]). These maps are then further gridded (to 4°x5°) and seasonally averaged to match the format of the aerosol radiative properties. Appendix figure A2 shows the seasonal maps of MODIS COD that were used in the calculation of $DARE_{OWC}$.

(5) **Aerosol and cloud layer heights** are assumed constant over the globe (respectively between 3-4km and 2-3km in this study), similar to other studies in Table 1 (e.g., Meyer et al. [2015]).

(6) **Earth's surface albedo** uses global gap-filled Terra and Aqua combined MODIS BRDF/albedo products. It uses the 16-day closest product (i.e., MCD43GF) to the middle of each season (i.e., Jan 15th for DJF, April 15th for MAM, July 15th for JJA and October 15th for SON). In the open ocean, the Cox and Munk [1954] sea surface albedo parameterization is applied with a wind speed of 10 ms^{-1}.

Using these inputs, **Daily $DARE_{OWC}$** results for each of the 4° x 5° grid cells are obtained by averaging 24 LibRadtran RT calculations, corresponding to 24 different sun positions at each hour of the day.

3. Results

3.1. AAC Occurrence Frequencies

To provide the necessary context for interpreting our TOA radiative transfer calculations, we first establish the observational AAC occurrence frequencies from which we will subsequently compute

Atmos. Chem. Phys. Discuss., https://doi.org/10.5194/acp-2018-1090
Manuscript under review for journal Atmos. Chem. Phys.
Discussion started: 6 November 2018

estimates of $DARE_{OWC}$. Figure 1 illustrates the annual gridded mean (5 years) global occurrence frequencies of a) single layer clouds, b) opaque water clouds that are suitable for the DR method and c) aerosol-above-clouds cases using the DR method. Figure 1d) shows the difference between the number of AAC cases using the DR method (i.e., number of cases with τ^{DR}_{AAC} >0) and the number of AAC cases using the standard Version 3 CALIOP product.

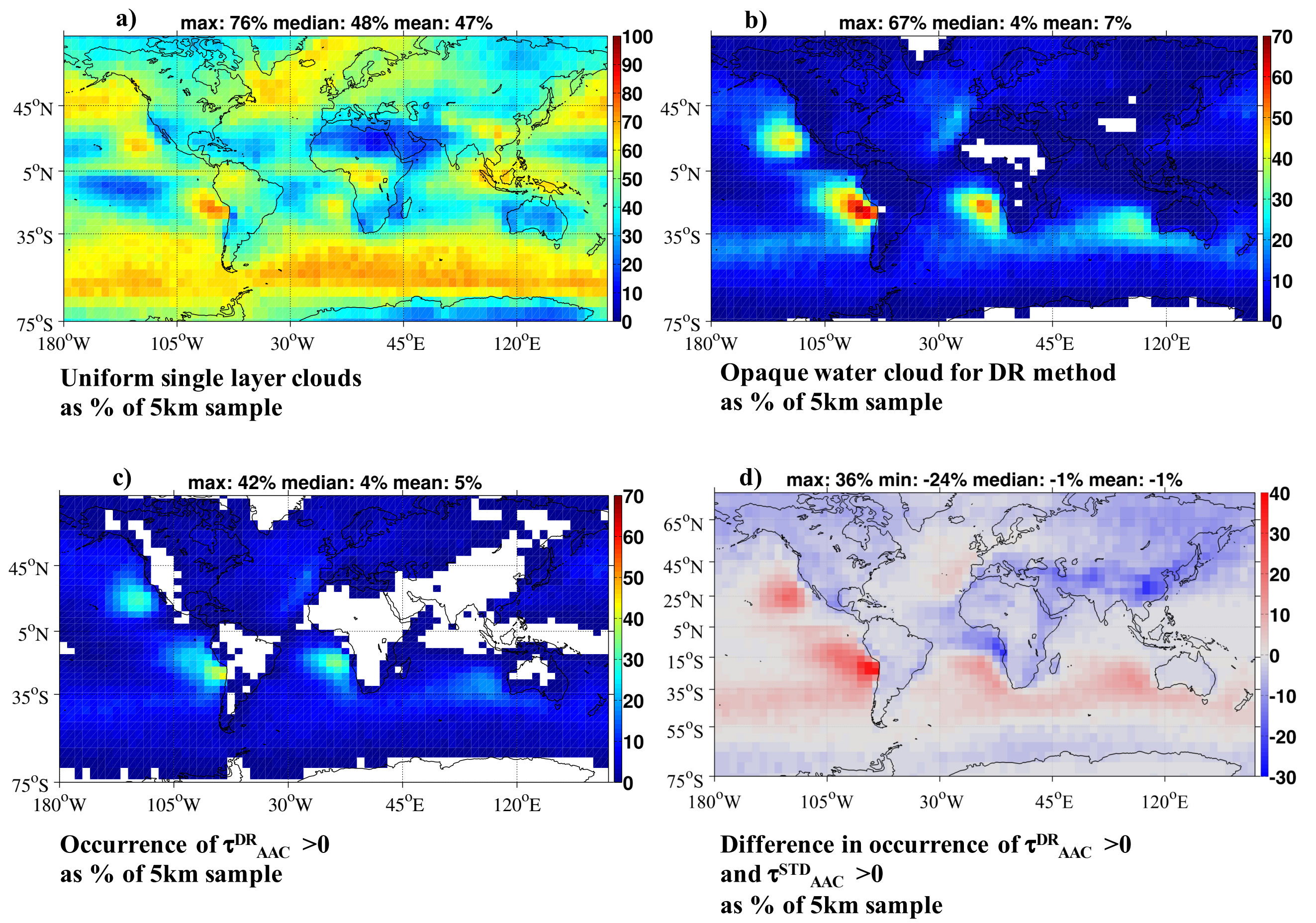

Figure 1: During nighttime, from 2008 to 2012 on a 4ºx5º-grid: Occurrence frequencies of (a) uniform single layer clouds (C1-C3 of Table B2), (b) opaque water clouds suitable for the DR method (C1-C5 of Table B2; these clouds can be obstructed or unobstructed) and (c) AAC cases that show a positive $\tau^{DR}{}_{AAC}$ at 532 nm. (d) shows the difference between the number of AAC cases using the DR method (i.e., number of cases with $\tau^{DR}{}_{AAC} > 0$) and the number of AAC cases using the standard Version 3 CALIOP product (i.e., number of cases with $\tau^{STD}{}_{AAC} > 0$); CALIOP AAC cases using the standard algorithm are defined as 5 km-columns showing an uppermost layer classified as aerosols and a cloud layer anywhere below that aerosol layer; the cloud itself does not have to satisfy any of the criteria of Table B2. Grid cells are 4º x 5º latitude/ longitude. The percentages in (a)-(d) use the number of 5 km CALIOP samples within each grid cell as a reference. White pixels show either no CALIOP observations, no CALIOP OWC detection, a small number of CALIOP unobstructed OWCs or a small number of positive $\tau^{DR}{}_{AAC}$ values. The title of each map shows the global maximum, median and mean values.

Uniform single layer clouds (i.e. C1-C3 of Table B2) are detected in ~47% of all 5 km CALIOP samples over the globe (see Figure 1(a)). In other words, at any one time, approximately half of the globe is covered by uniform single layer clouds. As expected, the highest occurrence of those clouds is in the high and low latitude bands and especially over the southern oceans. According to Figure 1(b), OWCs suitable for the DR method (i.e. C1-C5 of Table B2) are mostly in the marine stratocumulus regions and represent a mean of 7% of all 5 km CALIOP samples over the globe. This significant reduction from half-the-globe coverage is explained by the five criteria used to select OWCs for the application of the DR method (i.e., C1-C5 of Table B2). The highest occurrence of OWCs can be found offshore from the west coasts of North and South America, southwest Africa and Australia. In particular, OWC cover ranges from 60 to 75 % over the region of SE Atlantic in August [Klein and Hartmann, 1993]. Also, the southeastern Pacific region off the Peruvian and Chilean coasts is the location of the largest and most persistent stratocumulus deck in the world [Klein and Hartmann, 1993]. The percentage of AAC cases (i.e., AAC cases showing positive $\tau^{DR}{}_{AAC}$) at the basis of our study is very small compared to the total number of 5 km CALIOP profiles per grid cell (i.e. mean of 5% on Figure 1(c)). This is primarily due to a small number of low OWC used for the DR method over the globe (when comparing Figure 1(a) and 1(b)).

Figure 1(d) illustrates the difference in occurrence frequencies of AAC cases using the DR method compared to the standard Version 3 CALIOP product; negative (positive) values in blue (red) show the number of AAC cases that are missed (gained) by the DR method compared to using the standard CALIOP products. Unlike Figure 1(c), the AAC cases in Figure 1(d) that use the CALIOP standard product do not require any assumptions on the nature of the underlying cloud. Figure 1(d) shows that we could be missing (in blue) AAC cases over most of the land surfaces and over the Arabian Sea, the Tropical Atlantic and the SE Atlantic regions by using the DR method instead of the standard CALIOP product. One reason for the lack of AAC cases offshore from the west coast of Africa in our dataset is the filtering out of "unobstructed" but potentially aerosol-contaminated OWCs (see section B3 in the appendix for more details). However, some regions such as the NE and SE Pacific exhibit up to 40% more (in red) AAC cases when using the DR method. The SE Pacific region, especially offshore from

Atmos. Chem. Phys. Discuss., https://doi.org/10.5194/acp-2018-1090
Manuscript under review for journal Atmos. Chem. Phys.
Discussion started: 6 November 2018

Chile, shows particularly tenuous aerosols, with attenuated backscatter values that typically fall below the CALIOP detection limit and, hence, hampers the detection of AAC using the standard CALIOP algorithm [Kacenelenbogen et al., 2014].

In the rest of this study, the frequency of occurrence of AAC, f_{AAC}, is defined as:

$$f_{AAC} = N_{AAC}/N_{OWC} \qquad \text{Eq. (3)}$$

where N_{AAC} is the number of AAC cases (i.e., cases showing a positive $\tau^{DR}{}_{AAC}$ at 532nm) and N_{OWC} is the number of OWCs within each 4°x5° grid cell. Let us note that different studies use different references when computing the frequency of occurrence of AAC. The definition in Eq. (3) is similar to the one in Zhang et al. [2016] (see their Eq. (1)) and different from Devasthale and Thomas [2011], where f_{AAC} is defined as the ratio of AAC cases to the total number of CALIOP observations (similar to what is shown on Fig. 1(c)).

Figure 2 illustrates the global seasonal f_{AAC} (see Eq. 3) from 2008 to 2012. We find a median global f_{AAC} of 58% to 61% with regional values that can reach more than 80% in some regions such as the SE Atlantic, especially during the JJA season. The AAC occurrence frequencies in Fig. 2 generally agree with previous findings [Zhang et al., 2016; Devasthale and Thomas, 2011] on the location and season of highest f_{AAC}.

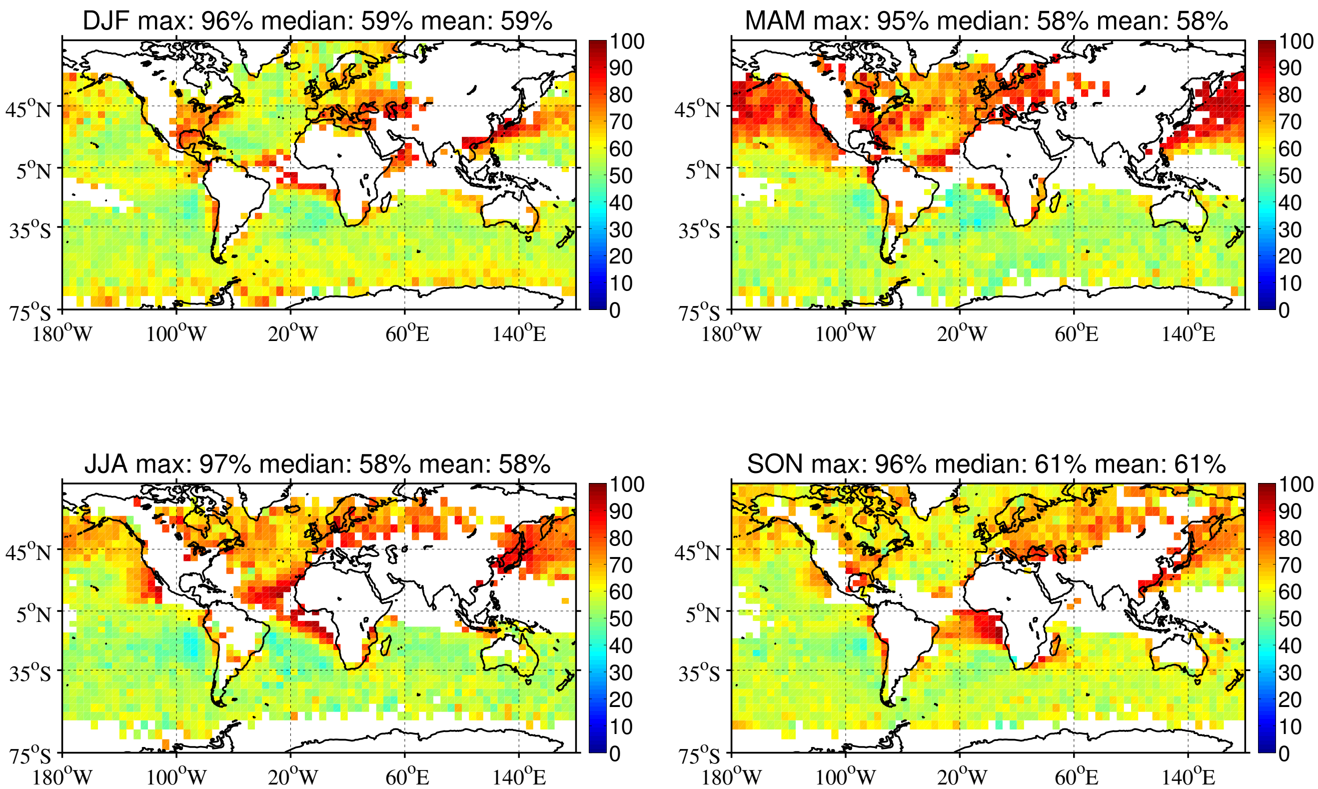

Figure 2: Global seasonal 4°x5° nighttime AAC occurrence frequency (noted f_{AAC}, see Eq. (3)) from 2008 to 2012. White pixels show either no CALIOP observations, a limited number of CALIOP unobstructed OWCs or a limited number of positive $\tau^{DR}{}_{AAC}$ values. White pixels are not considered in the global mean and median f_{AAC} values in the title of each map. The title of each map shows the global maximum, median and mean values.

3.2. AAC Optical Depths, Extinction-to-Backscatter Ratios and South Atlantic Anomaly Effects

3.2.1 AAC Optical Depths

Figure 3 introduces the global, nighttime and multi-year (2008-2012) AAC optical depths ($\tau^{DR}{}_{AAC}$, see Eq. 2) dataset that was computed in this study.

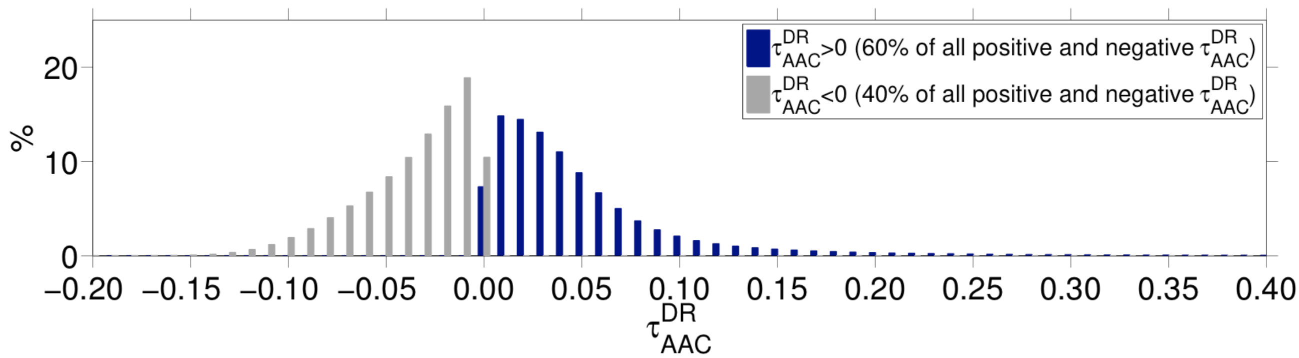

Figure 3: Global distribution of $\tau^{DR}{}_{AAC}$ at 532 nm. Positive (i.e., valid) $\tau^{DR}{}_{AAC}$ values are in dark blue (N~3.4M) and negative $\tau^{DR}{}_{AAC}$ values in grey (N~2.2M). These are nighttime CALIOP measurements from 2008-2012.

About 40% (i.e. 2.2M data points) of the initial dataset (i.e. N~5.6M) shows negative $\tau^{DR}{}_{AAC}$ values and were flagged as invalid data (see Figure 3, in grey). When looking at all valid (i.e. positive) $\tau^{DR}{}_{AAC}$ values (blue), we show a majority of very small $\tau^{DR}{}_{AAC}$ values in the 0.01-0.02 AOD range. This agrees with the findings of Devasthale and Thomas [2011]. Let us note that averaging all data points per 4°x5° grid cell (instead of the native resolution shown on Fig. 3) increases the AOD bin of maximum AAC occurrence globally from 0.01 (Fig. 3) to 0.03.

Table 3 shows four different ways of computing global seasonal and annual averages of aerosol optical depth above clouds: we use either τ^{DR}_{AAC} or τ^{DR}_{AAC} x f_{AAC} (see Case I-II or III-IV) and then either (i) exclude all cases of $\tau^{DR}_{AAC} < 0$ from the average (i.e., as in Case I and Case III), or (ii) set all cases of $\tau^{DR}_{AAC} < 0$ to zero, and include these samples in the averages (i.e., as in Case II and Case IV). Let us note that using τ^{DR}_{AAC} x f_{AAC} (instead of τ^{DR}_{AAC}) acknowledges the fact that some OWCs present no overlying aerosols. In this case, we assume that when the DR technique retrieves an invalid AAC measurement, $f_{AAC} = 0$ and there are no aerosols above the cloud.

Table 3: Global seasonal and annual averages of τ^{DR}_{AAC} (Case I and II) or τ^{DR}_{AAC} x f_{AAC} (Case III and IV) when assuming either (i) $\tau^{DR}_{AAC} < 0$ cases are excluded from the averages (Case I and III) or (ii) $\tau^{DR}_{AAC} < 0$ cases are set to zero and included in the averages (Case II and IV). Annual averages here (last column) are the mean of the seasonal averages.

Global mean aerosol optical depth	DJF	MAM	JJA	SON	Annual
Case I τ^{DR}_{AAC}, invalid τ^{DR}_{AAC} excluded	0.04	0.05	0.05	0.05	0.05
Case II τ^{DR}_{AAC}, invalid τ^{DR}_{AAC} =0	0.02	0.02	0.02	0.02	0.02
Case III τ^{DR}_{AAC} x f_{AAC}, invalid τ^{DR}_{AAC} excluded	0.03	0.03	0.04	0.03	0.03
Case IV τ^{DR}_{AAC} x f_{AAC}, invalid τ^{DR}_{AAC} x f_{AAC} =0	0.01	0.01	0.01	0.01	0.01

Figure 4 shows global seasonal nighttime median τ^{DR}_{AAC} x f_{AAC} from 2008 to 2012 (i.e., as in Case III of Table 3). The title of each seasonal map (respectively DJF, MAM, JJA, SON) in Figure 4 shows the

Atmos. Chem. Phys. Discuss., https://doi.org/10.5194/acp-2018-1090
Manuscript under review for journal Atmos. Chem. Phys.
Discussion started: 6 November 2018

Atmospheric Chemistry and Physics Discussions
Open Access

global maximum (respectively 0.11, 0.13, 0.22, 0.20), median (0.02 for all seasons) and mean (0.03 in DJF, MAM and SON and 0.04 in JJA) τ^{DR}_{AAC} x f_{AAC} values.

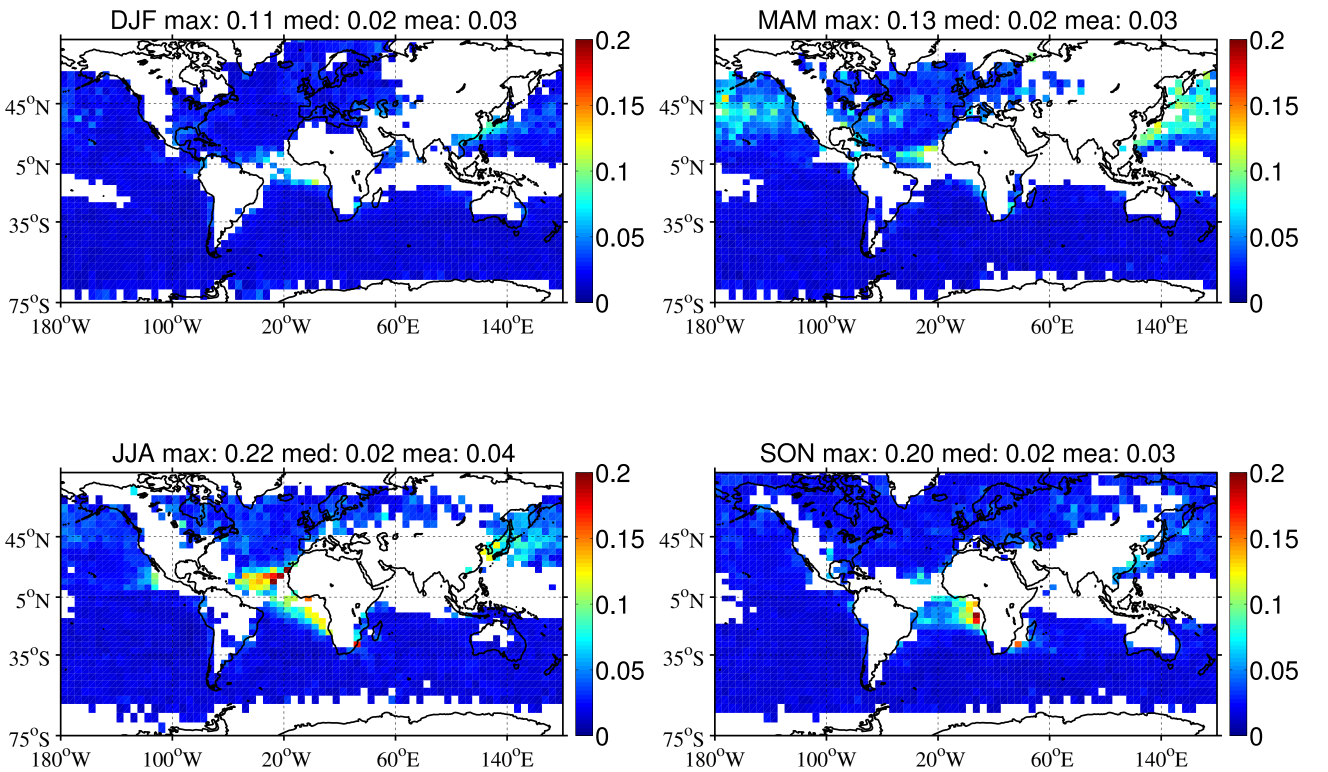

Figure 4: Global seasonal 4°x5° nighttime median τ^{DR}_{AAC} x f_{AAC} from 2008 to 2012. Underlying clouds satisfy the criteria in Table B2. White pixels show either no CALIOP observations, a limited number of CALIOP unobstructed OWCs or a limited number of positive τ^{DR}_{AAC} values. White pixels are not included when calculating the global mean and median τ^{DR}_{AAC} values in the title of each map (i.e., as in Case III in Table 3). Note that if the white pixels were set equal to zero, the seasonal and annual global

Atmos. Chem. Phys. Discuss., https://doi.org/10.5194/acp-2018-1090
Manuscript under review for journal Atmos. Chem. Phys.
Discussion started: 6 November 2018

τ^{DR}_{AAC} values would correspond to Case IV in Table 2. The title of each map shows the global maximum, median and mean values.

We do not expect the τ^{DR}_{AAC} x f_{AAC} values of Figure 4 to be similar to the results of [Zhang et al., 2014, Devasthale and Thomas, 2011, Alfaro-Contreras et al., 2016 or Yu and Zhang, 2013] (see Table 2) as these studies use standard CALIOP Level 2 aerosol and cloud layer products for AAC observations, instead of using the DR method. On the other hand, the results of Figure 4 seem to be in qualitative agreement with the global AAC AOD derived from spaceborne POLDER observations [Waquet et al., 2013a]. Let us note that Waquet et al. [2013a] have to assume an underlying COD larger than 3 to ensure the saturation of the polarized light scattered by the cloud layer. Although Deaconu et al. [2017] make different assumptions in the application of the DR method on CALIOP measurements (e.g., they impose a constant cloud lidar ratio for OWCs with clear air above), they find that POLDER and CALIOP τ^{DR}_{AAC} are in good agreement over the SE Atlantic ($R^2 = 0.83$) and over the Tropical Atlantic ($R^2 = 0.82$) from May to October 2008.

3.2.2. Extinction-to-Backscatter Ratios

Figure 5 illustrates global seasonal gridded nighttime median AAC extinction-to-backscatter ratio (S_{AAC}) values from 2008 to 2012 (section 2.2. describes the calculation of S_{AAC}). Bréon [2013] uses POLDER's specific directional signature close to the backscatter direction to derive aerosol extinction-to-backscatter values over the globe. Figure 4 of Bréon [2013], although in clear-sky conditions

Atmos. Chem. Phys. Discuss., https://doi.org/10.5194/acp-2018-1090
Manuscript under review for journal Atmos. Chem. Phys.
Discussion started: 6 November 2018

(compared to above OWCs in our case), seems to be in qualitative agreement with Figure 5. However, Bréon [2013] seems to not detect sufficient aerosol signals in the SE Pacific region to reach any conclusions.

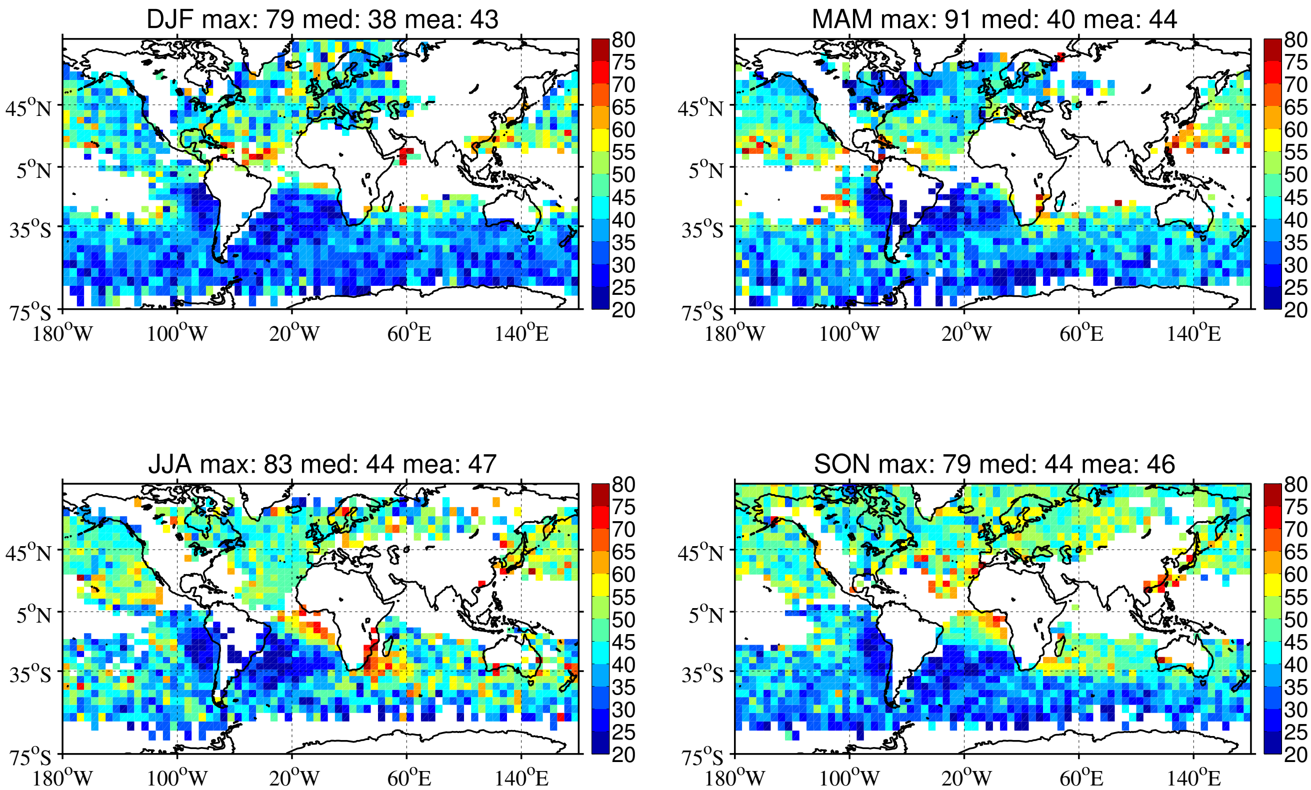

Figure 5: Global seasonal 4°x5° nighttime median S_{AAC} at 532 nm (sr) from 2008 to 2012. Underlying clouds satisfy the criteria in Table B2. White pixels show a limited number of CALIOP OWCs, positive τ^{DR}_{AAC} or valid S_{AAC} values (i.e. positive value, the solution has converged and/or the relative difference in τ^{DR}_{AAC} is below 0.01). White pixels are not considered in the global mean and median S_{AAC} values in the title of each map. The title of each map shows the global maximum, median and mean values.

Atmos. Chem. Phys. Discuss., https://doi.org/10.5194/acp-2018-1090
Manuscript under review for journal Atmos. Chem. Phys.
Discussion started: 6 November 2018

Atmospheric Chemistry and Physics Discussions

For reference, Table B3 in the appendix lists values of aerosol extinction-to-backscatter (lidar) ratios at 532 nm for different aerosol types (e.g. marine, urban industrial pollution, desert dust, polluted dust, biomass burning) reported in the literature. According to Table B3 and the global mean S_{AAC} values in Fig. 5 (i.e., 43-47 sr in the titles of each map), the aerosol type over OWCs that seems the most common over the globe during nighttime of 2008-2012 is mineral dust. On the one hand, a primary source of aerosols to the TAt region is dust from the Sahara, which can be transported over several thousands of kilometers and reach Central America and the Amazon basin, [Liu et al., 2008, 2015; Herman et al., 1997; Haywood et al., 2003; Waquet et al., 2013a, Zhang et al., 2016]. Over TAt, the season of highest f_{AAC} (i.e., ~80% in Fig. 2) and f_{AAC} x $\tau^{DR}{}_{AAC}$ (~0.1-0.2 in Fig. 4) is JJA and this season also shows a mean S_{AAC} of ~50 ± 3 sr (in Fig. 5), which is consistent with the predominance of Saharan dust (see Table B3). On the other hand, a primary aerosol source for the SEAt region is biomass burning from South Africa (see references in Table 1 and 2 for AAC over SEAt). SEAt shows higher mean S_{AAC} values (i.e., above 60 sr in Fig. 5) in JJA, reflecting the presence of biomass burning smoke aerosols (see Table B3). Let us note that S_{AAC} values in our study are slightly lower than in [Liu et al., 2015] (i.e., ~70 sr) over the SEAt region. This is most likely due to our approach to filtering the OWC lidar ratios used in the DR method (see Fig. B3 in the appendix).

3.2.3 South Atlantic Anomaly Effects

Atmos. Chem. Phys. Discuss., https://doi.org/10.5194/acp-2018-1090
Manuscript under review for journal Atmos. Chem. Phys.
Discussion started: 6 November 2018

The South Atlantic Anomaly (SAA) region in Fig. 5, defined within [50ºS, 0ºS; 90ºW, 40ºE], shows particularly low S_{AAC} results. One would expect to see higher S_{AAC} values in, for example, the SE Pacific (SEPa) region, as the aerosols in the region are predominantly mixtures of urban/biofuels (composed of a majority of sulfate aerosols), biomass burning, marine, and/or mixes of smelter emissions and mineral dust from the Atacama Desert [Chand et al., 2010; Blot et al., 2013]. The SAA is where the Earth's inner Van Allen radiation belt is the closest to the Earth's surface (at an altitude of ~200 km). This region is characterized by radiation-induced noise spikes in the CALIOP signal that are especially noticeable at nighttime (Hunt et al., 2009; Noel et al., 2014) and lead to high biases in the CALIOP integrated attenuated backscatter, which, in turn, lead to low biases in the CALIOP S_{AAC} values in the SAA.

Further investigation has shown (Fig. 6) a lower peak in the S_{AAC} values (~20sr) when these S_{AAC} values are associated with low τ^{DR}_{AAC} values (i.e., <0.05) and within the SAA region (in purple), compared to a peak around ~30 sr outside of the SAA region on Fig. 6 (in green).

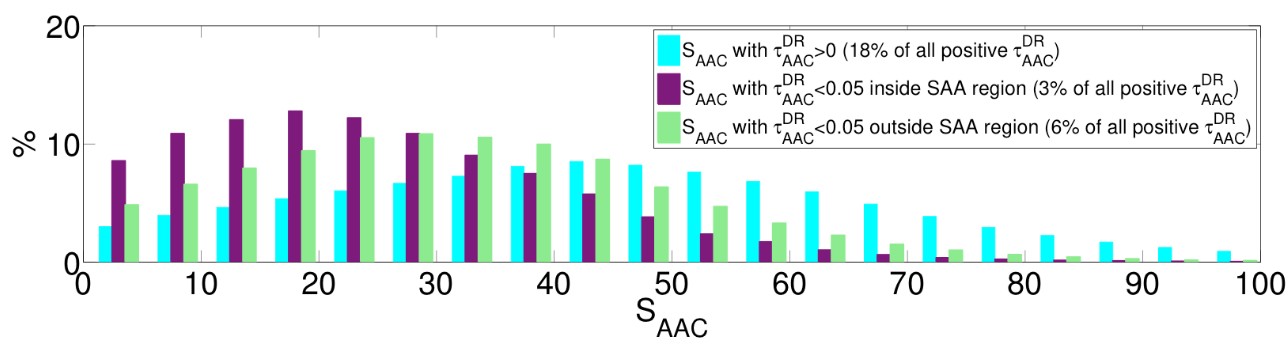

Figure 6: Global distribution of S_{AAC} at 532 nm. S_{AAC} values for all positive (i.e., valid) $\tau^{DR}{}_{AAC}$ values are in turquoise (N~0.63M, 18% of all positive $\tau^{DR}{}_{AAC}$ results), S_{AAC} values for $\tau^{DR}{}_{AAC} < 0.05$ inside the South Atlantic Anomaly (SAA, defined within [50ºS, 0ºS; 90ºW, 40ºE]) region are in purple (N~0.10M, 3% of all positive $\tau^{DR}{}_{AAC}$ results) and S_{AAC} values associated to $\tau^{DR}{}_{AAC} < 0.05$ outside the SAA region are in green (N~0.22M, 6% of all positive $\tau^{DR}{}_{AAC}$ results). These are nighttime CALIOP measurements from 2008-2012.

3.3. AAC Direct Aerosol Radiative Effects

3.3.1. Global results of $DARE_{OWC}$

Figure 7 shows the seasonal TOA SW $DARE_{OWC}$ estimates ($W \cdot m^{-2}$) that use CALIOP $\tau^{DR}{}_{AAC}$ x f_{AAC} (see Fig. 4) as input to a radiative transfer model, together with the other parameters described in section 2.2. $DARE_{OWC}$ in Fig. 7 is set equal to zero (i.e., white pixels) if $DARE_{OWC}$ is invalid or missing.

Atmos. Chem. Phys. Discuss., https://doi.org/10.5194/acp-2018-1090
Manuscript under review for journal Atmos. Chem. Phys.
Discussion started: 6 November 2018

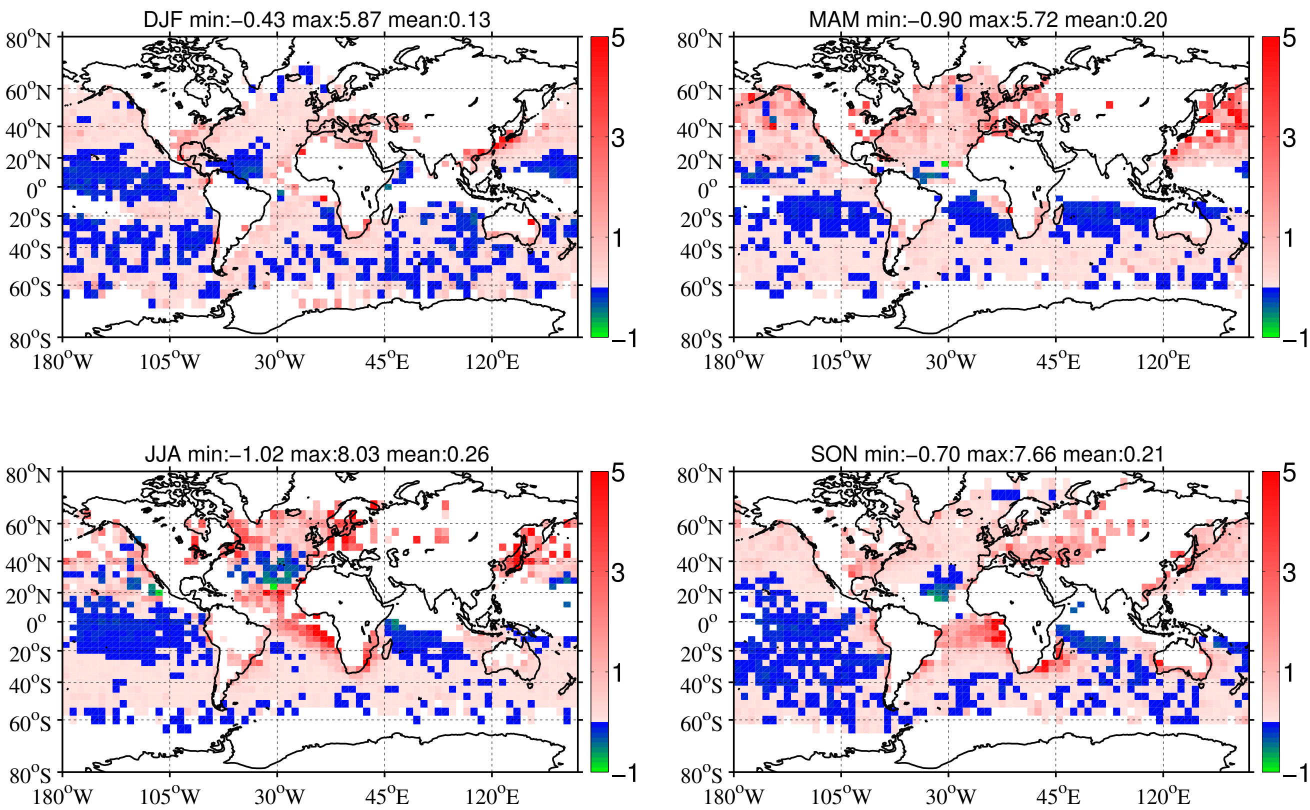

Figure 7: Global seasonal 4°x5° TOA SW $DARE_{OWC}$ estimates ($W \cdot m^{-2}$, as described in section 2.2). A white pixel is counted as $DARE_{OWC}=0$ in the global mean $DARE_{OWC}$ values in the title of each map. White pixels show a limited number of CALIOP OWCs, positive $\tau^{DR}{}_{AAC}$ values or auxiliary MODIS-OMI-CALIOP combined satellite observations. The title of each map shows the global minimum, maximum, and mean values.

Atmos. Chem. Phys. Discuss., https://doi.org/10.5194/acp-2018-1090
Manuscript under review for journal Atmos. Chem. Phys.
Discussion started: 6 November 2018

Similar to TOA $DARE_{cloudy}$ values from combined A-Train satellites in Oikawa et al. [2013] (see their Fig. 10) and from General Circulation Models (GCMs) (e.g. SPRINTARS) in Shulz et al. [2006] (see their Fig. 6 and 7), TOA $DARE_{OWC}$ values in Fig. 7 are mostly positive (i.e., a warming effect due to less energy leaving the climate system) over the globe. We find, globally, 72% positive 4ºx5º $DARE_{OWC}$ values (i.e., N=4045) against 28% negative values (i.e., N=1581) when considering all four seasons on Fig. 7. On the other hand, the highest negative TOA $DARE_{OWC}$ values on Fig. 7 (i.e., cooling effects shown in green pixels) are over the Tropical Atlantic (in MAM, JJA and SON), in the Pacific Ocean offshore from Mexico (in JJA) and at the periphery of the Arabian Sea (in JJA).

There are multiple ways to compute the global seasonal and annual $DARE_{cloudy}$ averages (i.e., $DARE_{OWC}$ in our case), and it is not clear which method would bring us closer to the true $DARE_{cloudy}$ state of the planet. For this reason, we list several different methods in Table 5. We either use CALIOP τ^{DR}_{AAC} or CALIOP τ^{DR}_{AAC} x f_{AAC} (Case I-II or III-IV) and we either exclude invalid $DARE_{OWC}$ values or set invalid $DARE_{OWC}$ = 0 (Case I-III or II-IV). For completeness and as an intermediate step towards $DARE_{all\text{-}sky}$ (see Eq. 1), Case V and VI show the global seasonal averages of $DARE_{OWC}$ x Cloud Fraction (CF), instead of $DARE_{OWC}$. The CF values use monthly MODIS AQUA MYD08_M3 products (variable "Cloud Retrieva Fraction Liquid FMean"), which are seasonally averaged and 4ºx5º-gridded.

Table 5: Global seasonal and annual averages of TOA SW $DARE_{OWC}$ estimates ($W{\cdot}m^{-2}$, as described in section 2.2). Annual averages (last column) are the mean of the seasonal averages (e.g., 0.53 for Case I is the average of 0.34, 0.52, 0.71 and 0.56); CF stands for Cloud Fraction.

Global averaged $DARE_{cloudy}$ ($W \times m^{-2}$)	DJF	MAM	JJA	SON	Annual
Case I $DARE_{OWC}$, $\tau^{DR}{}_{AAC}$, invalid $DARE_{OWC}$ excluded	0.34	0.52	0.71	0.56	0.53
Case II $DARE_{OWC}$, $\tau^{DR}{}_{AAC}$, invalid $DARE_{OWC}$=0	0.19	0.26	0.35	0.29	0.27
Case III $DARE_{OWC}$, $\tau^{DR}{}_{AAC}$ x f_{AAC}, invalid $DARE_{OWC}$ excluded	0.24	0.40	0.53	0.40	0.39
Case IV $DARE_{OWC}$, $\tau^{DR}{}_{AAC}$ x f_{AAC}, invalid $DARE_{OWC}$=0	0.13	0.20	0.26	0.21	0.20
Case V $DARE_{OWC}$ x CF, $\tau^{DR}{}_{AAC}$, invalid $DARE_{OWC}$ excluded	0.11	0.16	0.25	0.19	0.18
Case VI $DARE_{OWC}$ x CF, $\tau^{DR}{}_{AAC}$ x f_{AAC}, invalid $DARE_{OWC}$=0	0.04	0.06	0.09	0.07	0.07

Global seasonal and annual $DARE_{OWC}$ averages (see titles in Fig. 7 and Table 5) in our study represent the surface area of each grid cell. Each valid $DARE_{OWC}$ value per pixel on each map of Fig. 7 is multiplied by the surface of the pixel. These values per grid cell are then summed up and divided by the sum of the surface of all valid grid cells.

Figure 7 corresponds to the setting of Case IV in Table 5. The reason why we have selected to showcase this setting is because it closely resembles the settings of the $DARE_{cloudy}$ calculations in Zhang et al. [2016]; i.e., it assumes DARE = 0 when CALIOP cannot detect an aerosol layer. Figure 7 shows positive global seasonal $DARE_{OWC}$ averages between 0.13 and 0.26 $W \cdot m^{-2}$ (and an annual average of 0.20 $W \cdot m^{-2}$ in Table 5) as well as the lowest $DARE_{OWC}$ values when compared to $DARE_{OWC}$

values from Case I through Case IV in Table 5. These values are nonetheless much larger than the global annual ocean $DARE_{cloudy}$ values reported in Zhang et al. [2016] and Schulz et al. [2006] (e.g., annual average of 0.015 $W \times m^{-2}$ reported over ocean in Zhang et al. [2016]). Moreover, Matus et al. [2015] find (see their Table 2) a global TOA $DARE_{cloudy}$ value of 0.1 $W{\cdot}m^{-2}$ over thick clouds (these clouds are similar to our study), compensated by a global TOA $DARE_{cloudy}$ value of -2 $W{\cdot}m^{-2}$ over thin clouds.

Section 3.3.2 further analyzes $DARE_{OWC}$, together with f_{AAC}, $\tau^{DR}{}_{AAC}$, SSA, and COD results in a few selected regions and compares these results to previous studies.

3.3.2. Regional results of $DARE_{OWC}$

The f_{AAC} results in Fig. 2 help us define six major AAC "hotspots" over the North East Pacific (NEPa), South East Pacific (SEPa), Tropical Atlantic (TAt), South East Atlantic (SEAt), Indian ocean, offshore from West Australia (InWA), and North West Pacific (NWPa). To assist in the analysis of the remaining figures in this study, Figure 8 and Table 6 briefly describe these six AAC hotspots.

Atmos. Chem. Phys. Discuss., https://doi.org/10.5194/acp-2018-1090
Manuscript under review for journal Atmos. Chem. Phys.
Discussion started: 6 November 2018

Atmospheric Chemistry and Physics
Open Access
EGU
Discussions

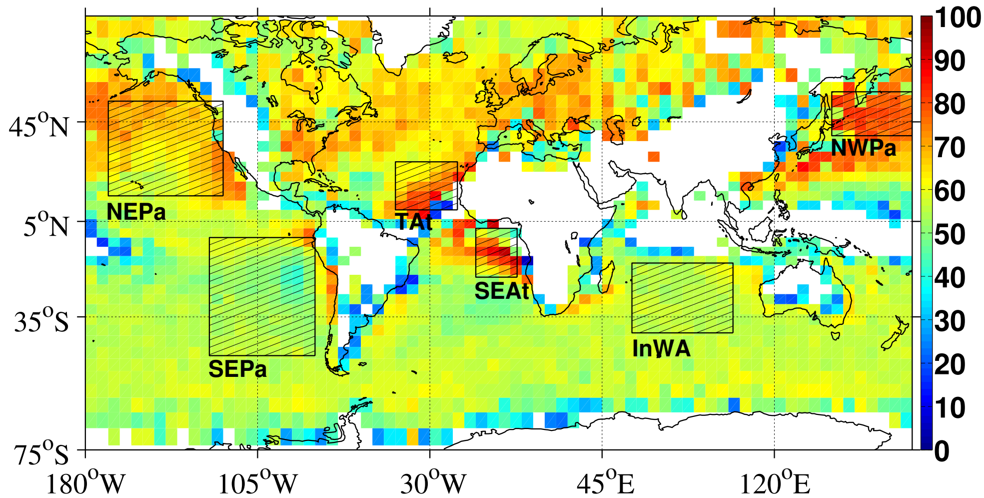

Figure 8: Six regions of high AAC occurrence, further defined in Table 6. Background map is the global annual 4° x 5° nighttime AAC occurrence frequency (f_{AAC}, see Eq. 3 and Fig. 2 for seasonal f_{AAC} maps). Global annual maximum, median and mean f_{AAC} values are respectively 93%, 57% and 57%.

Table 6: Six regions of high AAC occurrence (see Fig. 8), their season of highest AAC occurrence and its corresponding mean f_{AAC} value

Region	[latitude; longitude]	Season of most f_{AAC}
North East Pacific Ocean (NEPa)	[16N, 52N; 170W, 120W]	MAM (80%)
South East Pacific Ocean (SEPa)	[49S, 2S; 126W, 80W]	DJF (55%)
Tropical Atlantic Ocean (TAt)	[10N, 30N; 45W, 18W]	JJA (80%)
South East Atlantic Ocean (SEAt)	[19S, 2N; 10W, 8E]	SON (87%)
Indian Ocean, offshore from West Australia (InWA)	[41S, 13S; 58E, 102E]	SON (60%)
North West Pacific Ocean (NWPa)	[40N, 55N; 145E, 180E]	MAM (90%)

Atmos. Chem. Phys. Discuss., https://doi.org/10.5194/acp-2018-1090
Manuscript under review for journal Atmos. Chem. Phys.
Discussion started: 6 November 2018

Figure 9a illustrates the mean regional, seasonal or annual estimates of SW TOA $DARE_{OWC}$ ($W \cdot m^{-2}$) in each region of Table 6. Figure 9b-9f show the primary parameters used in the $DARE_{OWC}$ calculations (see section 2.2): the mean regional, seasonal or annual (b) percentage of grid cells that show valid (i.e., positive) f_{AAC} x $\tau^{DR}{}_{AAC}$ values compared to the total number of 4º x 5º pixels in each region, (c) CALIOP f_{AAC} values, (d) CALIOP f_{AAC} x $\tau^{DR}{}_{AAC}$ values, (e) assumed overlying SSA values at 546.3 nm and (f) assumed underlying COD values from MODIS.

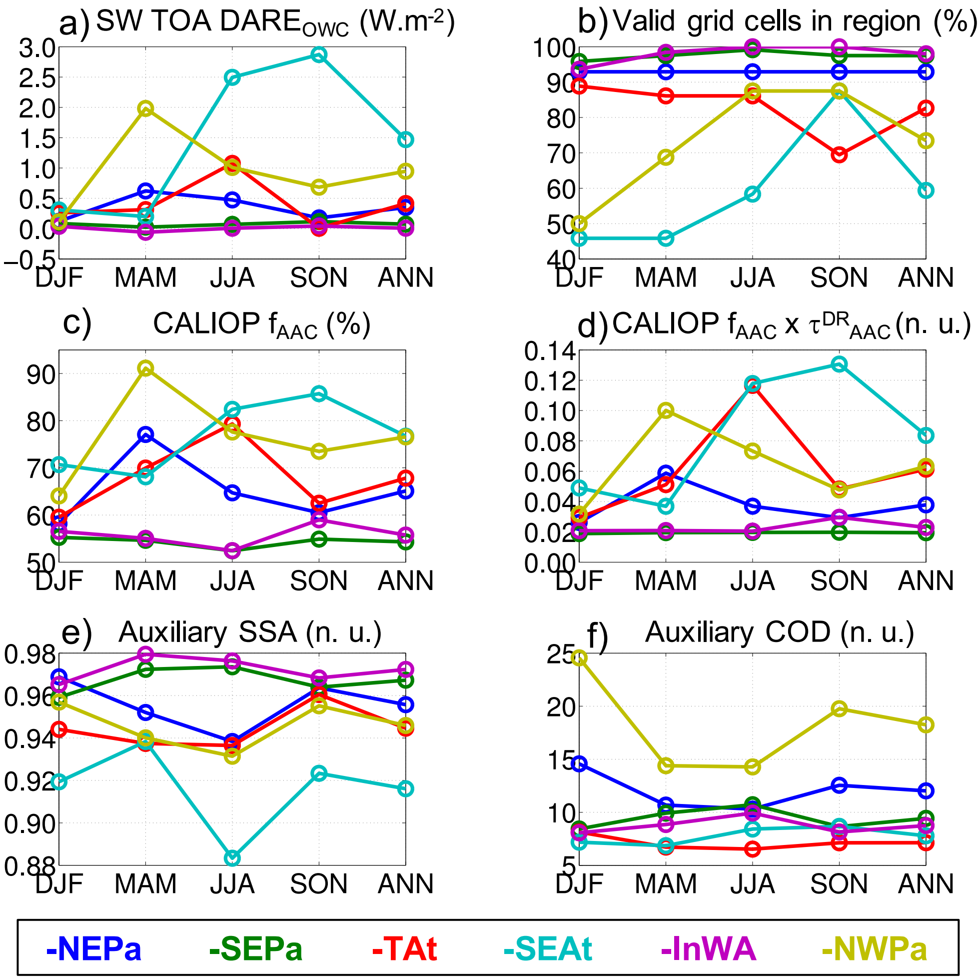

Figure 9: Mean regional, seasonal or annual (a) estimated SW TOA DARE$_{OWC}$ (W·m^{-2}, calculation is described in section 2.2), (b) percentage of grid cells that show valid f_{AAC} x τ^{DR}_{AAC} (i.e., positive) values compared to the total number of 4° x 5° pixels in each region, (c) CALIOP f_{AAC} (%), (d) f_{AAC} x τ^{DR}_{AAC} (no unit), (e) assumed overlying SSA at 546.3 nm from a combination of MODIS-OMI-

CALIOP and (f) assumed underlying COD from MODIS in each region of Table 6. $DARE_{OWC}$ in (a) is computed using the case IV of Table 5.

Table 7 reports the estimated seasonal or annual, regional range, mean and standard deviations of our TOA $DARE_{OWC}$ dataset (i.e., values of Fig. 9a)

Table 7: Estimated SW TOA $DARE_{OWC}$ (W·m^{-2}, setting is case IV of Table 5) in each region of Table 6.

Region	min, max	mean DJF	mean MAM	mean JJA	mean SON	mean ANN
NEPa	-0.57, 5.10	0.12±0.18	0.62±0.79	0.47±0.78	0.18±0.25	0.35 ± 0.50
SEPa	-0.21, 2.85	0.09±0.19	0.02±0.15	0.07±0.37	0.12±0.44	0.07 ± 0.29
TAt	-1.02, 5.25	0.26±0.43	0.31±0.43	1.08±1.66	0.01±0.42	0.41 ± 0.74
SEAt	0.20, 7.59	0.31±1.09	0.20±0.41	2.49±2.54	2.87±2.33	1.47 ± 1.59
InWA	-0.39, 0.83	0.04±0.16	-0.06±0.10	0.01±0.11	0.04±0.27	0.01 ± 0.16
NWPa	0.07, 5.72	0.11±0.14	1.98±1.85	1.01±1.65	0.68±0.46	0.95 ± 1.02

We record positive TOA $DARE_{OWC}$ values above 1 W·m^{-2} in Fig. 9a over TAt in JJA (1.08 ± 1.66), SEAt in JJA and SON (2.49 ± 2.54 and 2.87 ± 2.33) and NWPa in MAM (1.98 ± 1.85). Let us note that the highest positive TOA $DARE_{OWC}$ values on Fig. 9a and in Table 7 may not be entirely representative of each region, because they are based on a smaller number of valid $DARE_{OWC}$ results (86% valid values in JJA in TAt, 58-88% in JJA-SON in SEAt and 69% in MAM in NWPa). SEAt and NWPa are the only regions showing an all-positive range of $DARE_{OWC}$ values in Table 7 (i.e., respectively within

0.20 and 7.59 and within 0.07 and 5.72 W·m^{-2}). The spread (i.e., standard deviation) on those mean regional DARE$_{OWC}$ is of the same order of magnitude as the mean values themselves. For example, although TAt shows an annual mean DARE$_{OWC}$ value of 0.41 W·m^{-2}, most points (i.e., about 68%, assuming a normal distribution of DARE$_{OWC}$) are within 0.41 ± 0.74 W·m^{-2} (see Table 7). Those regions and seasons of highly positive DARE$_{OWC}$ values are associated with the highest CALIOP $\tau^{DR}{}_{AAC}$ x f_{AAC} values (see Fig. 9d: 0.12 in JJA in TAt, 0.12-0.13 in JJA-SON in SEAt and 0.10 in MAM in NWPa). They are also associated with lower SSA values (i.e., < 0.94 in Fig. 9e), typical of more light absorbing aerosols such as biomass burning. The underlying COD values are fairly constant (between ~5-10 on Fig. 9f), except for a noticeably higher COD over the NWPa region (between ~15-25 on Fig. 9f). NWPa is the region of highest latitudes in our study (i.e., between 40N and 55N). More variation in the COD at higher latitudes is also observed in Fig. A2 in the Appendix. This agrees with King et al. [2013], who show a larger zonal variation of COD (and increased uncertainty in the MODIS cloud property retrievals) in the higher latitudes of both hemispheres, particularly in winter (see their Fig. 12b).

When computing mean DARE$_{OWC}$ results within the "SE Atlantic" region defined in Zhang et al. [2016] (i.e., [30S, 10N; 20W, 20E] instead of [19S, 2N; 10W, 8E] in our study), we find a small fraction of valid pixels (i.e., an average of ~37%) but a mean annual DARE$_{OWC}$ value of 0.57 W·m^{-2}, which resides within their range of annual DARE$_{cloudy}$ values (i.e., 0.1 to 0.68 W·m^{-2} in Zhang et al. [2016]). Similar to Matus et al. [2015], the season of highest DARE$_{OWC}$ is SON over the SE Atlantic (they find 10% of DARE$_{OWC}$ larger than 10 W·m^{-2} over thick clouds with COD > 1, see their Fig. 9d). However, our DARE$_{OWC}$ results are significantly higher than the ones in Zhang et al. [2016] in our

SEAt region (defined as a smaller region and offshore from the "SE Atlantic" region in Zhang et al. [2016]) as well as in the TAt (similar latitude/ longitude boundaries to the ones of region "TNE Atlantic" in Zhang et al. [2016]) and the NWPa (similar boundaries to "NW Pacific" in Zhang et al. [2016]) regions.

We emphasize that the $DARE_{OWC}$ estimates in this study are not directly comparable to many previous studies (see Table 1) because of different spatial domain, period, satellite sensors and associated uncertainties. This will lead to the detection of different fractions of AAC above different types of clouds and different AAC types over the globe. The calculations of $DARE_{cloudy}$ can also differ greatly depending on different AAC aerosol radiative properties assumptions above clouds (especially absorption) and different assumptions in aerosol and cloud vertical heights (see Table 1).

Apart from the major differences in methods and sensors, it seems reasonable to say that we are missing AAC cases over pure dust-dominant regions such as the Arabian Sea or the TAt region (compared to e.g. Zhang et al. [2016] and Matus et al. [2015]). Both Matus et al. [2015] and Zhang et al. [2016] use the CALIOP Level 2 standard products to distinguish among a few aerosol types and infer specific aerosol optical properties in their $DARE_{cloudy}$. According to Figure 1(d), SEAt, TAt and the Arabian Sea are regions where we might be missing up to 40% of AAC cases when using the DR technique compared to the CALIOP standard products. The number of potentially missing AAC cases in our study is larger over the Arabian sea ([0-30ºN and 40-80ºE] due to the limited number of OWCs suitable for the DR method (see section B3 in the Appendix). Zhang et al. [2016] show that pure dust aerosols over these dust-dominant regions tend to produce a negative $DARE_{cloudy}$ when the underlying COD is below

~7 and this is the case for most of the clouds over these regions in their study. In summary, two factors in the DR method seem to hamper the detection of AAC in these regions: the low cloud optical depths of underlying clouds and very few cases of "clear air" above clouds. As a consequence, we propose that the positive $DARE_{OWC}$ values in our study should, in reality, be counter-balanced by more negative dust-driven $DARE_{cloudy}$ values over regions such as TAt and the Arabian Sea. On the other hand, the $DARE_{cloudy}$ results from Matus et al. [2015] and Zhang et al. [2016] might also differ from the true global $DARE_{cloudy}$ state of the planet for different reasons. As described in Matus et al. [2015], using CALIOP Level 2 standard products as in Matus et al. [2015] and Zhang et al. [2016] could lead to possible misclassification of dust aerosols as clouds [Omar et al., 2009], specifically around cloud edges in the TAt region. Moreover, even if the AAC is correctly detected in Matus et al. [2015] and Zhang et al. [2016], the amount of AAC AOD might be biased low due to their use of the CALIOP Level 2 standard products [Kacenelenbogen et al., 2014].

4. Uncertainties in our DARE above cloud results and the path forward

4.1. Detecting and quantifying the true amount of AAC cases

Our study uses mainly CALIOP Level 1 measurements to detect aerosols above specific OWCs that satisfy the criteria given in Table B2. We suggest that the number of CALIOP profiles that contain aerosols over any type of cloud (instead of only OWCs in this study) should be informed by a combination of different techniques applied to CALIOP observations (e.g., the standard products, the DR and the CR technique). Airborne observations such as those from the ObseRvations of Aerosols above Clouds and their intEractionS (ORACLES) field campaigns are well suited for providing further guidance on when to apply which technique.

To the best of our knowledge, the true global occurrence of aerosols above any type of cloud remains unknown. This question cannot be entirely answered with the use of CALIOP observations only. We suggest that a more complete global quantification and characterization of aerosol above any type of cloud should be informed by a combination of AAC retrievals from CALIOP, passive satellite sensors (e.g. POLDER [Waquet et al., 2013a,b, Peers et al., 2015, Deaconu et al., 2017] and MODIS [Meyer et al., 2013, Zhang et al., 2014, 2016], see Table 2) and model simulations [Schulz et al., 2006].

4.2. Considering the diurnal variability of aerosol and cloud properties

While we consider the diurnal cycle of solar zenith angles in our $DARE_{cloudy}$ calculations, we use MODIS for underlying COD and cloud R_e information as well as a combination of MODIS, OMI and CALIOP for overlying aerosol properties (see section 2.2). By using A-Train satellite observations (i.e., the AQUA, AURA and CALIPSO platforms), with an overpass time of 1:30 PM local time at the Equator, we are only using a daily snapshot of cloud and aerosol properties and not considering their daily variability.

Min and Zhang [2014] show a strong diurnal cycle of cloud fraction over the SEAt region (i.e., a 5-year mean trend of diurnal cloud fraction using SEVIRI that varies from ~60% in the late afternoon to 80% in the early morning on their Fig. 4). According to Min and Zhang [2014] (see their Table 2), assuming a constant cloud fraction derived from MODIS/ AQUA generally leads to an underestimation (less positive) by ~16% in the $DARE_{all\text{-}sky}$ calculations (see Eq. 1). Further studies should explore the implications of diurnal variations of COD and cloud R_e on $DARE_{cloudy}$ results using, for example, geostationary observations from SEVIRI.

Daily variations of aerosol (intensive and extensive) radiative properties above clouds cannot be ignored either. Arola et al. [2013] and Kassaniov et al. [2013] both show that even when the AOD strongly varies during the day, the accurate prediction of 24h-average $DARE_{non-cloudy}$ requires only daily averaged properties. However, in the case of under-sampled aerosol properties, such as when using A-Train derived aerosol properties (this study), the error in the 24h-$DARE_{non-cloudy}$ can be as large as 100% [Kassaniov et al., 2013]. Xu et al. [2016] show that the daily mean TOA $DARE_{non-cloudy}$ is overestimated by up to 3.9 $W \cdot m^{-2}$ in the summertime in Beijing if they use a constant MODIS/ AQUA AOD value, compared to accounting for the observed hourly-averaged daily variability. Kassaniov et al. [2013] propose that using a simple combination of MODIS TERRA and AQUA products would offer a reasonable assessment of the daily averaged aerosol properties for an improved estimation of 24h-$DARE_{non-cloudy}$.

4.3. Considering the spatial and temporal variability of cloud and aerosol fields

We have used coarse resolution (i.e., 4°x5°) seasonally gridded aerosol and cloud properties in our $DARE_{OWC}$ calculations (see section 2.2). As a consequence, sub-grid scale variability (or heterogeneity) of cloud and aerosol properties has not been considered. This approach is similar to assuming spatially and temporally homogeneous cloud and aerosol fields in our $DARE_{OWC}$ results.

Marine Boundary Layer (MBL) clouds show significant small-scale horizontal variability [Di Girolamo et al., 2010; Zhang et al., 2011]. Using mean gridded COD in $DARE_{cloudy}$ calculations, for example, can lead to significant biases in $DARE_{cloudy}$ calculations, an effect called the "plane-parallel albedo bias" [e.g., Oreopoulos et al., 2007, Di Girolamo et al., 2010, Zhang et al., 2011, Zhang et al., 2012]. Min and Zhang [2014] show that using a mean gridded COD significantly overestimates (by ~10% over the SEAt region) the $DARE_{cloudy}$ results when the cloud has significant sub-grid horizontal heterogeneity. Furthermore, this overestimation increases with increasing AOD, COD and cloud inhomogeneity. Future studies should examine the difference between $DARE_{cloudy}$ results calculated with gridded mean COD and cloud R_e values (this study) and $DARE_{cloudy}$ results calculated with MODIS Level-3 joint histograms of MODIS COD and cloud R_e (e.g., similar to Min and Zhang [2014]).

Aerosol spatial variation can be significant over relatively short distances of 10 to 100km, depending on the type of environment [Anderson et al., 2003; Kovacs, 2006; Santese et al., 2007; Shinozuka and Redemann, 2011; Schutgens et al., 2013]. Shinozuka and Redemann [2011] argue that only a few environments can be more heterogeneous than the Canadian phase of the ARCTAS (Arctic Research of the Composition of the Troposphere from Aircraft and Satellites) experiment where the airmass was subject to fresh local biomass emissions. In this type of environment, they observed a 19% variability of the AOD over a 20 km length (comparable in scale to a ~0.1°x0.1° area). They also found a 2% variability in the AOD over the same length in a contrasting homogeneous environment that occurred after a long-range aerosol transport event. As a consequence, similar to using a mean gridded underlying COD and cloud R_e, using mean gridded overlying aerosol radiative properties could very well bias our $DARE_{OWC}$ results.

Atmos. Chem. Phys. Discuss., https://doi.org/10.5194/acp-2018-1090
Manuscript under review for journal Atmos. Chem. Phys.
Discussion started: 6 November 2018

As a preliminary investigation into the sources and magnitudes of these potential biases, we have used TOA $DARE_{non\text{-}cloudy}$ (see Eq. 1) estimates derived using well-collocated aerosol properties (hereafter called "retrieve-then-average" or R-A) from a companion study (Redemann et al. [2018]; see section A of the appendix) and compared those to $DARE_{non\text{-}cloudy}$ estimates computed using seasonally gridded mean aerosol properties at seasonally gridded mean vertical heights (hereafter called "average-then-retrieve" or A-R). Both $DARE_{non\text{-}cloudy}$ results obtained with the two methods are compared over ocean and at a resolution of 4°x5°.

A majority (i.e., ~58%) of A-R $DARE_{non\text{-}cloudy}$ results are within ±35% of the R-A $DARE_{non\text{-}cloudy}$ results. We find very few (i.e., ~1%) negative R-A $DARE_{non\text{-}cloudy}$ values paired with positive A-R $DARE_{non\text{-}cloudy}$ values and very few large differences between both methods (i.e., less than 1% of the differences are above ±10W m^{-2}). However, we find a weak agreement between A-R and R-A $DARE_{non\text{-}cloudy}$ values during each of the seasons (i.e., a correlation coefficient between 0.21 and 0.34). The A-R $DARE_{non\text{-}cloudy}$ values are generally biased high relative to the R-A calculations, as illustrated by positive mean and median values of the A-R to R-A differences (respectively 0.64 W m^{-2} and 0.92 W m^{-2}; standard deviation of 2.25). When computing the global seasonal mean A-R and R-A $DARE_{non\text{-}cloudy}$ values separately, we find that the global seasonal A-R $DARE_{non\text{-}cloudy}$ values overestimate the global seasonal R-A $DARE_{non\text{-}cloudy}$ values by 17%, 19%, 21%, and 17% in DJF, MAM, JJA and SON. Moreover, the seasonal median A-R $DARE_{non\text{-}cloudy}$ values overestimate the seasonal median R-A $DARE_{non\text{-}cloudy}$ values in all six regions of Table 6 (i.e., median differences between 0.28 W m^{-2} in NWPa in SON and 3.05 W m^{-2} in SEAt in JJA). The geospatial distributions of these differences in DARE calculation strategies are illustrated in Figure 10.

Atmos. Chem. Phys. Discuss., https://doi.org/10.5194/acp-2018-1090
Manuscript under review for journal Atmos. Chem. Phys.
Discussion started: 6 November 2018

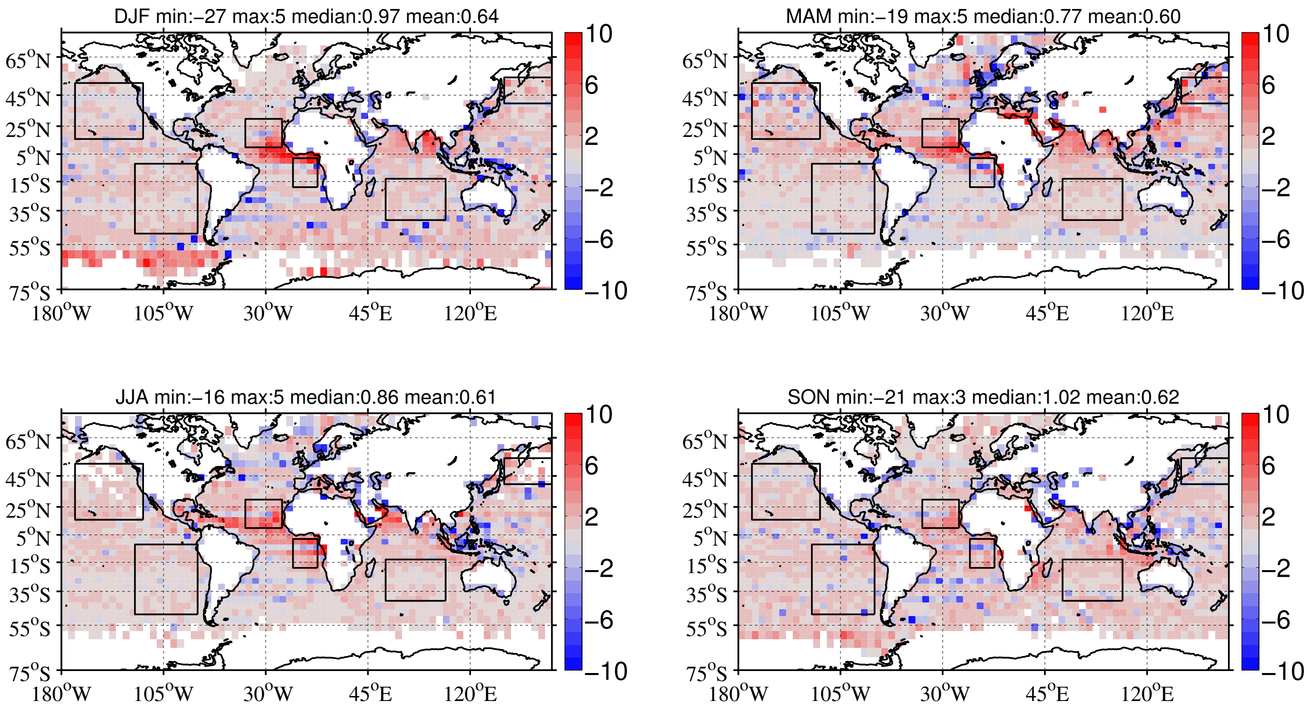

Figure 10: Seasonal maps showing the differences in SW TOA DARE$_{non\text{-}cloudy}$ computed using the average-then-retrieve (A-R) and the retrieve-then-average (R-A) strategies. Positive values (in red) show regions where the A-R DARE calculations are larger, whereas negative values (in blue) show regions where the R-A DARE calculations are larger. The squares show different regions defined in Table 6. The title of each map shows the global minimum, maximum, median and mean values.

4.4. Assuming similar intensive aerosol properties above clouds and in near-by cloud-free skies

In the calculation of $DARE_{OWC}$, we assume similar intensive aerosol properties above clouds and in near-by clear skies. This assumption might not be valid and should be investigated in future studies by comparing aerosol properties and their probability distributions over clear and cloudy conditions using observations from the ORACLES field campaign.

4.5. Assuming fixed aerosol and cloud vertical layers

Finally, aerosol and cloud layer heights are assumed constant over the globe in our study (see section 2.2). Matus et al. [2015] state that estimates of $DARE_{cloudy}$ over SEAt are highly sensitive to the relative vertical distribution of cloud and aerosols. Quijano et al. [2000], Penner et al. [2003] and Chung et al. [2005] demonstrate the importance of the vertical distributions of cloud and aerosol layers in an accurate estimate of radiative fluxes. Chung et al. [2005], for example, show that varying the relative vertical distribution of aerosols and clouds leads to a range of global modeled anthropogenic TOA $DARE_{all\text{-}sky}$ (see Eq. 1) from -0.1 to -0.6 $W \cdot m^{-2}$ (see their Table 2). Future studies should incorporate mean gridded (i.e., 4ºx5º in this study)-seasonal CALIOP Level 2 aerosol and cloud vertical profiles into the calculation of $DARE_{OWC}$.

5. Conclusions

We have computed a first approximation of global seasonal TOA short wave Direct Aerosol Radiative Effects (DARE) above Opaque Water Clouds (OWCs), $DARE_{OWC}$, using observation-based aerosol and cloud radiative properties from a combination of A-Train satellite sensors and a radiative transfer model. Our $DARE_{OWC}$ calculations make three major departures from previous peer-reviewed results: (1) they use extensive aerosol properties derived from the Depolarization Ratio, DR, method applied to

Atmos. Chem. Phys. Discuss., https://doi.org/10.5194/acp-2018-1090
Manuscript under review for journal Atmos. Chem. Phys.
Discussion started: 6 November 2018

Level 1 CALIOP measurements, whereas previous studies often use CALIOP Level 2 standard products which introduce higher uncertainties and known biases; (2) our $DARE_{OWC}$ calculations are applied globally, while most previous studies focus on specific regions of high AAC occurrence such as the SE Atlantic; and (3) our calculations use intensive aerosol properties retrieved from a combination of A-Train satellite sensor measurements (e.g., MODIS, OMI and CALIOP).

Our study agrees with previous findings on the locations and seasons of the maximum occurrence of AAC over the globe. We identify six regions of high AAC occurrence (i.e., AAC hotspots): South and North East Pacific (SEAt and NEPa), Tropical and South East Atlantic (TAt and SEAt), Indian Ocean offshore from West Australia (InWA) and North West Pacific (NWPa). We define $\tau^{DR}{}_{AAC}$, the Aerosol Optical Depth (AOD) above OWCs using the DR method on CALIOP measurements, f_{AAC}, the frequency of occurrence of AAC cases and, S_{AAC}, the extinction-to-backscatter (lidar) ratio above OWCs. We record a majority of $\tau^{DR}{}_{AAC}$ x f_{AAC} values at 532nm in the 0.01-0.02 range and that can exceed 0.2 over a few AAC hotspots. The majority of the S_{AAC} values lie in the 40 – 50 sr range, which is typical of dust aerosols. S_{AAC} is also consistent with typical dominant aerosol types over the TAt and SEAt regions (respectively dust and biomass burning).

We find positive averages of global seasonal $DARE_{OWC}$ between 0.13 and 0.26 W·m^{-2} and an annual global mean $DARE_{OWC}$ value of 0.20 W·m^{-2} (i.e., a warming effect on climate). Regional seasonal $DARE_{OWC}$ values range from -0.06 W·m^{-2} in the Indian Ocean, offshore from western Australia (in March-April-May) to 2.87 W·m^{-2} in the South East Atlantic (in September-October-November). High positive values are usually paired with high aerosol optical depths (>0.1) and low single scattering albedos (<0.94), representative of e.g. biomass burning aerosols.

Although the $DARE_{OWC}$ estimates in this study are not directly comparable to previous studies because of different spatial domain, period, satellite sensors, detection methods, and/ or associated uncertainties, we emphasize that they are notably higher than the ones from [Zhang et al., 2016; Matus et al., 2015 and Oikawa et al., 2013]. In addition to differences in satellite sensors, AAC detection methods, and the assumptions enforced in the calculation of $DARE_{cloudy}$, there are several other factors that may contribute to the overall higher $DARE_{OWC}$ values we report in this study. The most likely contributors are (1) a possible underestimate of the number of dust-dominated AAC cases; (2) our use of the DR method on CALIOP Level 1 data to quantify the AAC AOD; and, in particular, (3) the technique we have chosen for aggregating sub-grid aerosol and cloud spatial and temporal variability. We discuss each of these in turn in the following paragraphs.

Two factors seem to be preventing the DR method from recording enough AAC cases in these regions: the low cloud optical depths of underlying clouds and very few cases of “clear air” above clouds. The DR method used in this study is restricted to aerosols above OWCs that satisfy a long list of criteria. The AAC dataset in this study underestimates (i) the total number of CALIOP 5 km profiles that contain AAC over all OWCs (i.e., not just suitable to the DR technique), (ii) the total number of CALIOP 5 km profiles that contain AAC over any type of clouds over the globe and (iii) the true global occurrence of AAC over any type of clouds. To the best of our knowledge, the true amount of AAC in (i), (ii) and (iii) remains unknown. A better characterization of the “unobstructed” OWCs in the application of the DR technique on CALIOP measurements might bring us closer to answering (i). A combination of CALIOP standard, DR and CR techniques together with airborne observations (e.g., from the ORACLES field campaign) might answer (ii). Finally, (iii) cannot be answered with the only use of CALIOP observations. The results in this study should be combined with aerosol-above-cloud retrievals from passive satellite sensors (e.g. POLDER [Waquet et al., 2013a,b, Peers et al., 2015, Deaconu et al., 2017] or MODIS [Meyer et al., 2013, Zhang et al., 2014, 2016]) and model simulations [Schulz et al., 2006] to obtain a more complete global quantification and characterization of aerosol above any type of clouds.

Compared to other methods, the DR technique applied to CALIOP measurements retrieves $\tau^{DR}{}_{AAC}$ with fewer assumptions and lower uncertainties. Other global $DARE_{cloudy}$ results (e.g., Matus et al. [2015] and Zhang et al. [2016]) use CALIOP standard products to detect the AAC cases, quantify the AAC AOD and define the aerosol type (and specify the aerosol intensive properties). These studies rely on the presence of aerosol in concentrations sufficient to be identified by the CALIOP layer detection scheme, and on the ability of the CALIOP aerosol subtyping algorithm to correctly identify the aerosol type and thus select the correct lidar ratio for the AOD retrieval. While several recent studies have taken various approaches to quantifying the amount of aerosol currently being undetected in the CALIOP backscatter signals, their general conclusions are unanimous. The CALIOP standard products underestimate above-cloud aerosol loading and the corresponding AAC AOD (Kacenelenbogen et al., 2014; Kim et al., 2017; Toth et al., 2018; Watson-Parris et al., 2018), and this in turn leads to underestimates of both $DARE_{non\text{-}cloudy}$ and $DARE_{cloudy}$ (Thorsen and Fu, 2015; Thorsen et al., 2017).

Atmos. Chem. Phys. Discuss., https://doi.org/10.5194/acp-2018-1090
Manuscript under review for journal Atmos. Chem. Phys.
Discussion started: 6 November 2018

In this study, we have assumed spatially and temporally homogeneous clouds and aerosols in our $DARE_{OWC}$ calculations. As a preliminary investigation of such effects on our calculations, we have compared DARE calculations derived from well collocated aerosol properties (retrieve-then-average) to DARE calculations using seasonally gridded mean aerosol properties (average-then-retrieve). We have shown that the average-then-compute DARE results generally overestimate the retrieve-then-average results both on a global scale and in each of our selected regions. Further research and analysis are required to determine which of these two computational approaches provides the most accurate estimates of real-world DARE.

Appendix A: Method to obtain aerosol radiative properties in non-cloudy (i.e., clear-sky) conditions using MODIS, OMI and CALIOP and to estimate $DARE_{non\text{-}cloudy}$

A companion paper, Redemann et al. [2018], develops and refines a method for retrieving full spectral (i.e., at 30 different wavelengths) extinction coefficients, Single Scattering Albedo (SSA) and asymmetry parameters from satellite aerosol products in non-cloudy (i.e., clear-sky) conditions. The method requires colocation of quality-screened satellite data, selection of aerosol models that reproduce the satellite observations within stated uncertainties, and forward calculation of aerosol radiative properties based on the selected aerosol models. They use MODIS-Aqua AOD at 550 and 1240 nm, CALIPSO integrated backscattering (IBS) at 532 nm and OMI Absorption Aerosol Optical Depth (AAOD) at 388 nm (see Table A1). The aerosol radiative properties resulting from this method are called MOC retrievals (for MODIS-OMI-CALIOP).

Table A1. Data sets currently used for global MODIS-OMI-CALIOP (MOC) retrievals of aerosol radiative properties [Redemann et al., 2018]; DT: Dark Target and EDB: Enhanced Deep Blue.

Product	**Source**	**Assumed Uncertainties***	**Weight*,****
550 nm AOD	MODIS Collection 6 (Ocean, DT-Land, EDB-Land)	±5% ± 30 Mm^{-1}	0.1488
1240 nm AOD	MODIS Collection 6 (extrapolated spectrally over land)	±5% ± 30 Mm^{-1}	0.1422
388 nm AAOD	OMI (OMAERO for ocean, OMAERUV for DT-land), MODIS EDB	±30% ± 50 Mm^{-1}	0.5542
532 nm IBS	CALIPSO V3-01	±30% ± 0.1 $Mm^{-1}sr^{-1}$	0.1548

* For the values after division by CALIPSO layer depth

** The weight, w_i, is used to calculate the cost function $X = (\Sigma w_i((x_i - \hat{x}_i)/\delta\hat{x}_i)^2)^{1/2}$ where x_i are the retrieved parameters, $\hat{x}_i$ are the observables, $\delta\hat{x}_i$ are the uncertainties in the observables.

The choice of OMI satellite algorithms (see Table A1) reflects their assessment of the representativeness of subsampling OMI data along the CALIPSO track; i.e., they compared the probability distribution (PDF) of the OMI retrievals along the CALIPSO track to the global PDF and chose the data set that had the best match between global and along-track PDF for the over-ocean and two over-land data sets, the latter being different in their use of MODIS dark target (DT) versus enhanced Deep-Blue (EDB) data as the source of AOD. They collocate the MODIS and OMI products within a 40x40 km^2 box centered at each CALIPSO 5-km profile location after Redemann et al. [2012].

Atmos. Chem. Phys. Discuss., https://doi.org/10.5194/acp-2018-1090
Manuscript under review for journal Atmos. Chem. Phys.
Discussion started: 6 November 2018

For the OMAERUV data set, they choose the SSA product for the layer height indicated by the collocated CALIOP backscatter profile.

Their aerosol models emulate those of the MODIS aerosol over-ocean algorithm [Remer et al., 2005]. Like the MODIS algorithm, they define each model with a lognormal size distribution and wavelength-dependent refractive index. They then combine two of these models, weighted by their number concentration, and compute optical properties for the bi-modal lognormal size distribution. Unlike the MODIS algorithm, they allow combinations of two fine-mode or two coarse-mode models. They use ten different aerosol models, which stem from some of the MODIS over-ocean models [Remer et al., 2005] but include more absorbing models, which was motivated by application of their methodology to the Arctic Research of the Composition of the Troposphere from Aircraft and Satellites (ARCTAS) field campaign data, requiring more aerosol absorption than included in the current MODIS over-ocean aerosol models. They use MOC spectral aerosol radiative properties to then calculate Direct Aerosol Radiative Effects (i.e., $DARE_{non\text{-}cloudy}$, see Eq. 1) through a delta-four stream radiative transfer model with fifteen spectral bands from 0.175 to 4.0 μm in SW and twelve longwave (LW) spectral bands between 2850 and 0 cm^{-1} [Fu and Liou, 1992].

In order to use these MOC parameters (retrieved in clear-skies) in our $DARE_{OWC}$ calculations, we need to assume similar aerosol intensive properties in clear skies compared to above clouds and we need to spatially and/ or temporally grid these MOC parameters. As discussed in section 2.2, we use seasonally averaged MOC spectral SSA, aerosol asymmetry parameter, and extinction retrievals on 4°x5° grids. Figure A1 illustrates seasonal maps of MOC SSA used in our calculations of $DARE_{OWC}$.

Atmos. Chem. Phys. Discuss., https://doi.org/10.5194/acp-2018-1090
Manuscript under review for journal Atmos. Chem. Phys.
Discussion started: 6 November 2018

Atmospheric Chemistry and Physics
Open Access
Discussions

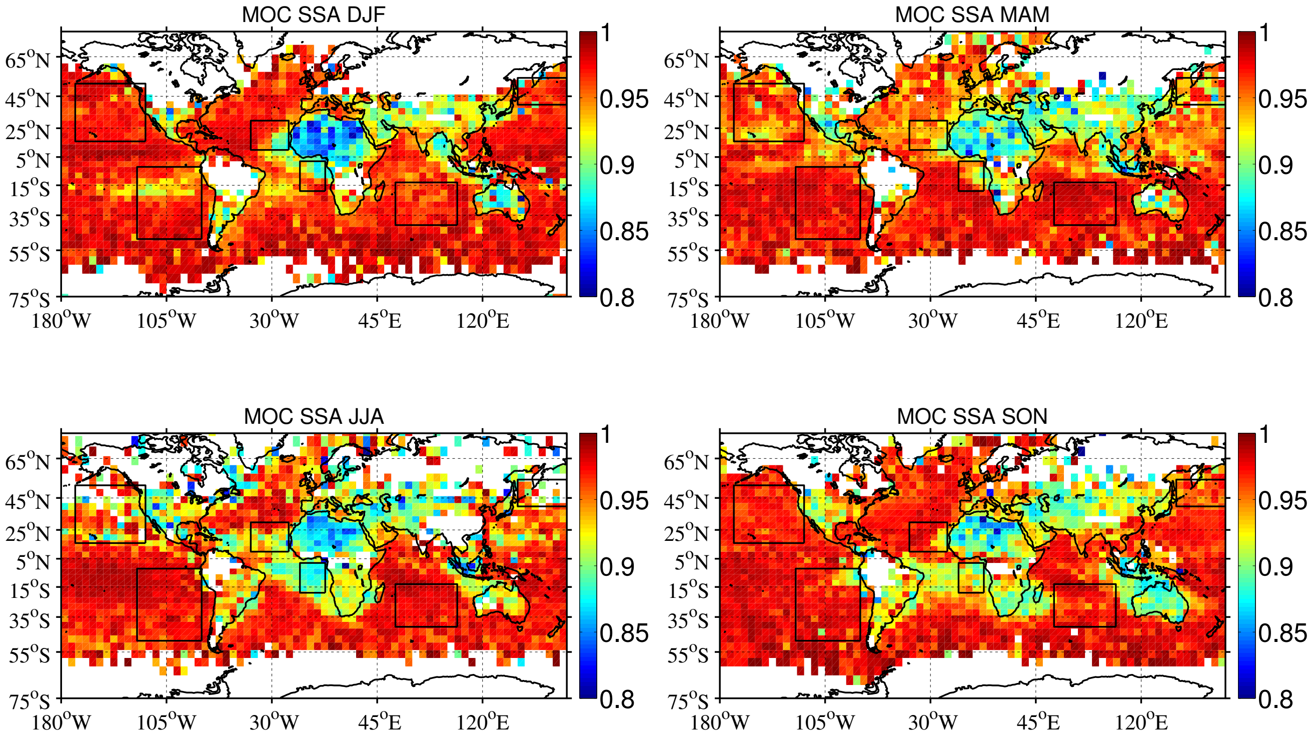

Figure A1: Seasonal maps of MOC SSA at 546.3 nm in 2007 used in the calculations of $DARE_{OWC}$. The squares show different regions defined in Table 6.

The $DARE_{OWC}$ calculations in our study also require information about the underlying cloud optical properties. As discussed in section 2.2, we use seasonally mean gridded COD from MODIS such as illustrated in Figure A2.

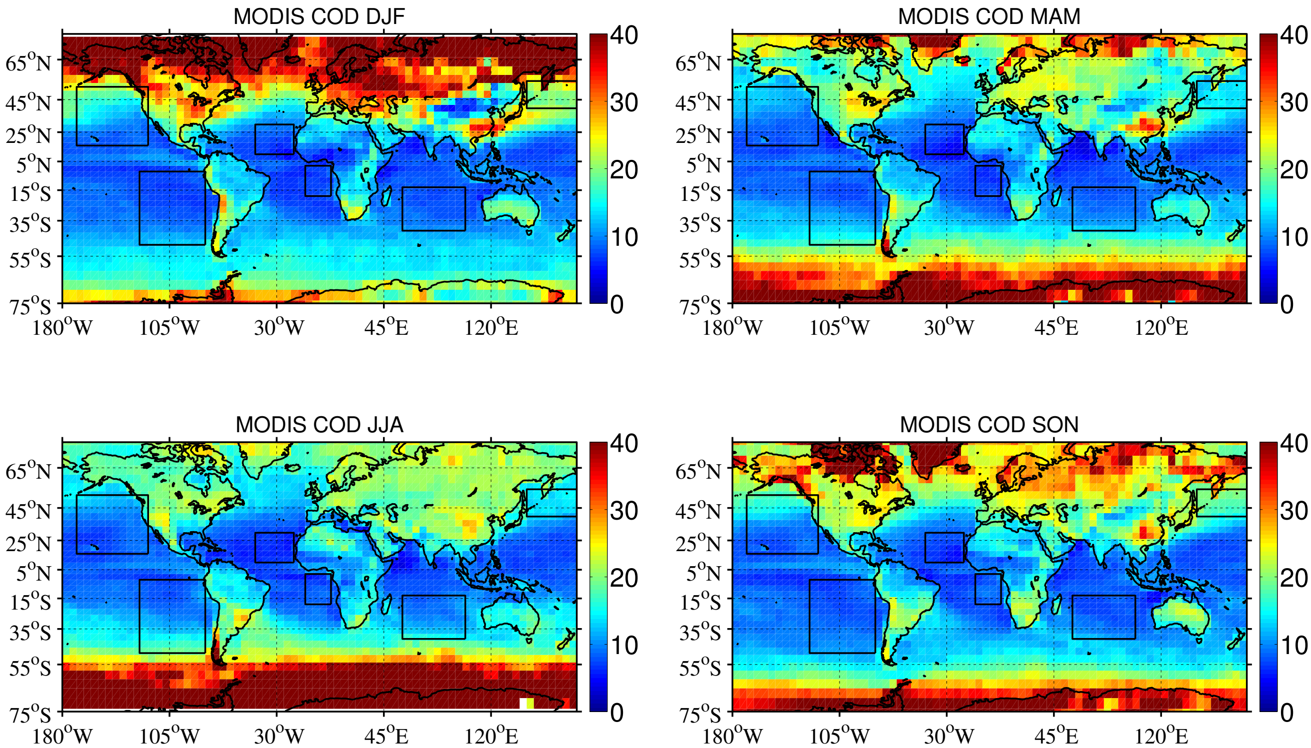

Figure A2: Seasonal maps of COD used in the calculations of $DARE_{OWC}$. COD information is inferred from MODIS seasonally averaged monthly 1°x1° grids (i.e. liquid water cloud products of MYD08_M3: "Cloud Effective Radius Liquid Mean Mean" and "Cloud Optical Thickness Liquid Mean Mean" [Platnick et al. 2015]) from 2008 to 2012. The squares show different regions defined in Table 6.

Appendix B: Method for AAC detection, AAC AOD and S_{AAC} computation

The depolarization ratio (DR) method [Hu et al., 2007b] used to derive estimates of the optical depths (τ) of aerosols above clouds (AAC) is given in Eq. (2) and repeated here for convenience:

$$\tau^{DR}{}_{AAC} = -0.5 \times \ln[IAB^{OWC}{}_{SS,AAC} / IAB^{OWC}{}_{SS,CAC}] \quad \text{(B1)}$$

The subscripts SS and CAC represent, respectively, 'single scattering' and 'clear above clouds'. $IAB^{OWC}{}_{SS}$ (i.e., either $IAB^{OWC}{}_{SS,AAC}$ or $IAB^{OWC}{}_{SS,CAC}$) is the single scattering integrated attenuated backscatter (IAB), derived from the product of the measured 532 nm attenuated backscatter coefficients integrated from cloud top to cloud base, IAB^{OWC}, and a layer effective multiple scattering factor, η^{OWC}, derived from the layer-integrated volume depolarization ratio of the water cloud (called δ^{OWC}) using:

$$\eta^{OWC} = [(1-\delta^{OWC})/(1+\delta^{OWC})]^2 \quad \text{(B2)}$$

[Hu et al., 2007a]. The single scattering IAB is thus derived using:

$$IAB^{OWC}{}_{SS,X} = \eta^{OWC} \times IAB^{OWC}{}_{measured,X} \quad \text{(B3)}$$

for both aerosol above cloud cases (X = AAC) and those cases with clear skies above (X = CAC). An assumption of the DR method is that δ^{OWC} is negligibly affected by any aerosols that lie in the optical path between the OWC and the lidar.

Table B1 provides a high-level overview of the procedure we use to compute aerosol optical depth ($\tau^{DR}{}_{AAC}$) and aerosol extinction-to-backscatter ratio (S_{AAC}) above OWCs over the globe. We chose to concentrate on night-time CALIOP observations only, as they have substantially higher signal-to-noise ratios (SNR) than the daytime measurements [Hunt et al., 2009].

Table B1: Steps required to compute $\tau^{DR}{}_{AAC}$ and S_{AAC}. $^{(*)}$: we construct global maps of 4 x 5° pixels using median values. Superscripts 1 and 2 denote respectively CALIOP Level 1 and Level 2 aerosol or cloud layer products.

Atmos. Chem. Phys. Discuss., https://doi.org/10.5194/acp-2018-1090
Manuscript under review for journal Atmos. Chem. Phys.
Discussion started: 6 November 2018

Step	Description	CALIOP, GEOS-5 and other computed products that are used in each step	More detail
S1	Select specific Opaque Water Clouds (OWC) suitable for the DR technique	CAD Score[2], Integrated Attenuated Backscatter Uncertainty 532[2], Integrated Volume Depolarization Ratio Uncertainty[2], Horizontal Averaging, Opacity Flag[2], Feature Classification Flags[2], Layer Top Altitude[2], Layer Top Temperature[2], Surface Wind Speed[2]	section B1, Table B2
S2	Select a subset of OWCs from (S1) with clear air above	Overlying Integrated Attenuated Backscatter 532[2], simulated molecular layer-integrated attenuated backscatter [Powell et al., 2002 and 2006] and OWCs from (S1)	section B2
S3	Process seasonal maps of median $IAB^{OWC}_{SS,CAC}$ and record number of $IAB^{OWC}_{SS,CAC}$ values per grid cell (*)	Integrated Attenuated Backscatter 532[2], Integrated Volume Depolarization Ratio[2], and OWCs with clear air above from (S2)	section B3
S4	Compute τ^{DR}_{AAC} along track	Total Attenuated Backscatter 532[1], Molecular Number Density[1], Ozone Number Density[1] Integrated Attenuated Backscatter 532[2,+], Integrated Volume Depolarization Ratio[2,+], Layer Top Altitude[2,+], Layer Base Altitude[2,+] and seasonal maps of $IAB^{OWC}_{SS,CAC}$ from (S3) Note: (+) these parameters are re-computed from CALIOP level 1 data, and may differ from the standard CALIOP products	Eq. (2) or Eq. (B1)
S5	Compute S_{AAC} along track	τ^{DR}_{AAC} from (S4), Total Attenuated Backscatter 532[1] and Molecular Number Density[1] Note: aerosol layer top is set at 12km and aerosol layer base is fixed at the range bin above the recalculated OWC layer top height	Eq. (15), [Fernald et al., 1972]
S6	Process seasonal maps of median τ^{DR}_{AAC} and S_{AAC} and record number of τ^{DR}_{AAC} and S_{AAC} values per grid cell (*)	τ^{DR}_{AAC} of (S4), S_{AAC} from (S5) and we filter using number of $IAB^{OWC}_{SS,CAC}$ values per grid cell and per season from (S3)	section 3.2

Atmos. Chem. Phys. Discuss., https://doi.org/10.5194/acp-2018-1090
Manuscript under review for journal Atmos. Chem. Phys.
Discussion started: 6 November 2018

Atmospheric Chemistry and Physics
Discussions

The first step (S1) is to identify OWCs that are suitable for the application of the DR method. The acceptance criteria used to identify these clouds are described below in section B1 and listed in Table B2. In the second step (S2), we use the overlying integrated attenuated backscatter (i.e., the 532 nm attenuated backscatter coefficients integrated from TOA to the OWC cloud tops) to partition the OWC into two classes: (i) "unobstructed" clouds, for which the magnitude of the overlying IAB suggests that only aerosol-free clear skies lie above; and (ii) "obstructed" clouds for which we expect to be able to retrieve positive estimates of $\tau^{DR}{}_{AAC}$. Section B2 describes the objective method we have developed to separate unobstructed clouds (for which we can compute $IAB^{OWC}{}_{SS,CAC}$) from obstructed clouds (for which we calculate $IAB^{OWC}{}_{SS,AAC}$).

In step (S3), we construct global seasonal maps of median $IAB^{OWC}{}_{SS,CAC}$ using 5 consecutive years (2008-2012) of CALIOP nighttime data (see section B3). By doing this we can subsequently compute estimates of $\tau^{DR}{}_{AAC}$ without invoking assumptions about the lidar ratios of water clouds in clear skies [Hu et al., 2007]. Throughout this study, we chose to compute global median values within each grid cell (instead of mean values) to limit the impact of particularly high or low outliers on our statistics.

In step (S4), we compute estimates of $\tau^{DR}{}_{AAC}$ for all obstructed OWC within each grid cell using Eq. (2) or Eq. (B1) and the 5-year nighttime seasonal median values of $IAB^{OWC}{}_{SS,CAC}$ from (S3) (i.e., each $\tau^{DR}{}_{AAC}$ value along the CALIOP track is computed using one median value of $IAB^{OWC}{}_{SS,CAC}$ per 4ºx5º pixel and per season).

For the OWCs considered in this study, true layer base cannot be measured by CALIOP, simply because the signal becomes totally attenuated at some point below the layer top. Instead, what is

Atmos. Chem. Phys. Discuss., https://doi.org/10.5194/acp-2018-1090
Manuscript under review for journal Atmos. Chem. Phys.
Discussion started: 6 November 2018

Atmospheric Chemistry and Physics
Open Access
Discussions

reported in the CALIOP data products is an apparent base, which indicates the point at which the signal was essentially indistinguishable from background levels. Numerous validation studies have established the accuracy of the CALIOP cloud layer detection scheme (e.g., McGill et al., 2007; Kim et al., 2011; Thorsen et al., 2011; Yorks et al., 2011; Candlish et al., 2013). Strong attenuation of the signal by optically thick aerosols above an OWC can, in some cases, introduce biases into the cloud height determination, which would lead to misestimates of $IAB^{OWC}_{SS,AAC}$ and subsequent errors in τ^{DR}_{AAC}. To ensure the use of consistent data processing assumptions throughout our retrievals of τ^{DR}_{AAC} and S_{AAC}, we recalculated the components of $IAB^{OWC}_{SS,AAC}$ (i.e., the "Integrated Attenuated Backscatter 532" and "Integrated Volume Depolarization Ratio") using parameters in the CALIOP Level 1 product ("Total Attenuated Backscatter 532", "Molecular Number Density" and "Ozone Number_Density") and optimized estimates of cloud top and base altitudes based on the "Layer Top Altitude" and "Layer Base Altitude" values reported in the CALIOP Level 2 layer product.

In step (S5), we compute the S_{AAC} above OWC by solving the two-component lidar equation given by Eq. (15) of Fernald et al. [1972], and (following Young et al., 2018) reproduced below as Eq. (B4):

$$S_{AAC} = \frac{1 - T^2_{AAC}(0,r_{top})\, T_m^{2\frac{S_{AAC}}{S_m}}(0,r_{top})}{2\int_0^{r_{top}} \beta'(r)\, T_m^{2(\frac{S_{AAC}}{S_m-1})}(0,r)\,dr} \qquad \text{(B4)}$$

$T^2_{AAC}(0,r)$ is the two-way aerosol two-way transmittance between the lidar (at range = 0) and range r. In our application, r_{top} is the range bin immediately above the OWC top altitude, so that

Atmos. Chem. Phys. Discuss., https://doi.org/10.5194/acp-2018-1090
Manuscript under review for journal Atmos. Chem. Phys.
Discussion started: 6 November 2018

$T^2_{AAC}(0,r_{top})=\exp(-2x\tau^{DR}_{AAC})$. $T_m(0,r)$ is the one-way transmittance due to molecular scattering and ozone absorption, S_m is the molecular extinction-to-backscatter ratio, $\beta'(r)$ is the attenuated backscatter coefficient at range r; i.e.,

$$\beta'(r)=(\beta'_m(r)+\beta'_{AAC}(r))xT^2_m(0,r)xT^2_{AAC}(0,r) \qquad \text{(B5)}$$

[Young and Vaughan, 2009]. Because the regions studied typically have very low aerosol loading, molecular scattering often contributes most of the signal hence the two-component lidar equation is required. Moreover, because equation (B4) is transcendental and cannot be solved algebraically, solutions are obtained using an iterative method. Valid S_{AAC} values must satisfy $\tau^{DR}_{AAC} > 0$ and $S_{AAC} > 0$, and the iteration much converge to a solution for which the relative difference between successive τ^{DR}_{AAC} estimates is less than 0.01 (i.e. $|(\tau^{DR}_{AAC} - \tau^{Fernald}_{AAC})/\tau^{DR}_{AAC}| < 0.01$).

Apart from the identification of specific OWCs in step (S1), the primary Level 2 CALIOP parameters used to calculate τ^{DR}_{AAC} (S2-S4 in Table B1) are (i) the integrated attenuated backscatter above cloud top to detect "clear air" cases (i.e. "Overlying Integrated Attenuated Backscatter 532" in step (S2)), (ii) the layer integrated attenuated backscatter of the OWC with clear air above (i.e. "Integrated Attenuated Backscatter 532" in step (S3)) and (iii) the cloud multiple scattering factor, derived as a function of the layer integrated volume depolarization ratio (i.e. the "Integrated Volume Depolarization Ratio" in S3 and S4).

Below, we list the potential sources of errors associated with those three products:

(a) the accuracy of the 532 nm channel calibrations,

Atmos. Chem. Phys. Discuss., https://doi.org/10.5194/acp-2018-1090
Manuscript under review for journal Atmos. Chem. Phys.
Discussion started: 6 November 2018

Atmospheric Chemistry and Physics
Open Access
Discussions

(b) the signal-to-noise ratio (SNR) of the backscatter data within the layer,

(c) the estimation of molecular scattering in the integrated attenuated backscatter (section 3.2.9.1 of the CALIPSO Feature Detection ATBD, http://www-calipso.larc.nasa.gov/resources/pdfs/PC-SCI-202_Part2_rev1x01.pdf), and

(d) the accuracy of the depolarization calibration (see section 5 in Powell et al., [2009]).

Concerning (a), Rogers et al. [2011] show that the NASA LaRC HSRL and CALIOP Version 3 532 nm total attenuated backscatter agree on average within ~3%, demonstrating the accuracy of the CALIOP 532 nm calibration algorithms.

Concerning (b), we assume the influence of the SNR returned from the OWC is negligible as the OWCs are strongly scattering features and our dataset is composed of nighttime data only. However, the backscatter from tenuous and spatially diffuse aerosol layers with large extinction-to-backscatter ratios can lie well beneath the CALIOP attenuated backscatter detection threshold. When such layers lie above OWCs, the measured overlying integrated attenuated backscatter can fall within one standard deviation of the expected 'purely molecular' value that is used to identify CAC (or "unobstructed") OWC in our dataset (S2; see Sect. B2). Within the context of this study, these tenuous and spatially diffuse aerosol layers can have appreciable AOD, and thus care must be taken to ensure that these sorts of cases are not misclassified as CAC OWC. Section B3 discusses such cases, possibly found, for example, over the region of SEAt.

B1. Select specific Opaque Water Clouds suitable for DR technique

Successful application of the DR method (Eq. 2 or Eq. B1) requires a very specific type of underlying cloud (step (S1) in Table B1). Table B2 lists the criteria we have applied to the CALIOP 5 km cloud layer products for the selection of these specific OWCs over the globe.

Table B2: Criteria used to select the Opaque Water Clouds (OWC) for the application of the DR method to obtain the AAC frequency of occurrence, AAC optical depth, AAC lidar ratio and $DARE_{OWC}$ in this study.

criteria	metric	interpretation
C1	Number of cloud layers = 1	a single cloud in each column
C2	High CALIOP cloud-aerosol discrimination (CAD) score ($90 \leq CAD \leq 100$) and high SNR (IAB SNR > 159, δ^{OWC} SNR > 2)	highly confident of cloud classification
C3	Cloud detected at 5 km averaging resolution with CALIOP single shot cloud cleared fraction = 0	cloud is spatially uniform over a 5 km averaging interval
C4	CALIOP opacity flag = 1; surface wind speed < 9 m/s	cloud is opaque
C5	CALIOP phase classification is high confidence water; $\delta^{OWC} < 0.5$; cloud top altitude < 3 km; cloud top temperature ≥ -10° C	highly confident of cloud phase identification (water)

We ensure that each cloud is the only cloud detected within the vertical column (C1) and is guaranteed to be of high quality by imposing filters on various CALIOP quality assurance flags (C2). Imposing the "single shot cloud cleared fraction = 0" in criterion (C3) assures that the clouds are uniformly detected at single shot resolution throughout the full 5 km (15 shot) horizontal extent. As a result, we will intentionally miss any broken clouds and any clouds that show a weaker scattering intensity within one or more laser pulses with the 15 shot average. On the other hand, enforcing the single shot cloud fraction = 0 criteria simultaneously ensures that all $\tau^{DR}{}_{AAC}$ values in this study will lie below a certain threshold: larger values would attenuate the signal to the point that single shot detection of underlying clouds is no longer likely. Consequently, some highly attenuating biomass burning events (e.g., with $\tau^{DR}{}_{AAC}$ >2.5) can be excluded from the cases considered here.

At high surface wind speeds over oceans, the CALIOP V3 layer detection algorithm may fail to detect surface backscatter signals underneath optically thick but not opaque layers. In such cases, CALIOP's standard algorithm may misclassify the column as containing an opaque overlying cloud. To avoid such scenarios, we exclude all the cases with high surface wind conditions (C4). Let us note that this condition was applied on the entire dataset, disregarding the surface type (i.e. land or ocean), as our OWC dataset resides mostly over ocean surfaces (see Figure 1b).

Criterion (C5) requires that the OWC be both low enough (cloud top below 3km) and warm enough (cloud top temperature above -10ºC as in Zelinka et al. [2012]) to ensure that it is composed of liquid water droplets. After applying all the criteria of Table B2, the median OWC top height of our dataset is ~1.6 km. According to Hu et al. [2009], any feature showing a cloud layer integrated volume depolarization ratio above 50% should correspond to an ice cloud with randomly oriented particles. Criterion (C5) assures the deletion of such cases.

The averaged single-layer, high QA, uniform cloud (i.e. C1-C3 in Table B2) has a top altitude of ~8 km, a top temperature around -38º C and mean surface winds of ~6 m s^{-1}. Selecting only those clouds with top temperatures above -10º C removes 30-40% of the observations. Subsequently filtering out clouds with top heights above 3 km removes an additional 30% of the observations. Finally, filtering out clouds with underlying winds above 9 m s^{-1} deletes another 20% of the observations. Among all single-layer, high QA, uniform clouds (i.e. C1-C3 in Table B2), we find that ~45-50% are opaque clouds (C4), and that ~11-12% satisfy all criteria (C1-C5) of Table B2.

B2. Select a subset of Opaque Water Clouds with clear air above

To distinguish between OWCs having clear skies above (i.e., unobstructed clouds, see S2 in Table B1) and those having overlying aerosols, we examine the overlying integrated attenuated backscatter reported in the CALIOP Level 2 cloud layer products. The total Integrated Attenuated Backscatter (IAB) value above a cloud (i.e., $IAB^{tot}_{aboveCloud}$) can be written as follows:

$$IAB^{tot}_{aboveCloud} = \int_0^{cloudtop} \left[\beta_a(r) T_a^2(0,r) T_m^2(0,r) \right] dr + \int_0^{cloudtop} \left[\beta_m(r) T_m^2(0,r) T_a^2(0,r) \right] dr \qquad \text{(B6)}$$

Here $\beta_a(r)$ and $\beta_m(r)$ are, respectively, the aerosol and the molecular backscatter coefficients (km^{-1} sr^{-1}) at range r (km), and $T^2_a(0,r)$ and $T^2_m(0,r)$ are the two-way transmittances between the lidar (at range r = 0) and range r due to, respectively, aerosols and molecules.

Figure B1 shows simulated profiles of the integrated attenuated backscatter above any given altitude, z, ($IAB^{mol}_{above\ z}$) for a purely molecular atmosphere for both daytime (solid green curve) and nighttime conditions (dashed green curve). These data were generated by the CALIPSO lidar simulator [Powell et al., 2002; Powell, 2005; Powell et al., 2006] using molecular and ozone number density profiles obtained from the GEOS-5 atmospheric data products distributed by the NASA Goddard Global Modeling and Assimilation Office (GMAO). The error envelopes at ±1 standard deviation (light blue curves) and ±1.5 standard deviation (dark blue curves) around the mean represent measurement uncertainties for CALIPSO profiles averaged to a nominal horizontal distance of 5 km. The mean $IAB^{mol}_{above\ z}$ profiles represent an average of all data along the CALIPSO orbit track on 17 March 2013 that began at 03:29:28 UTC and extended from 78.8°N, 20.3°E to 77.3°S, 77.0°W. Spot checks of mean $IAB^{mol}_{above\ z}$ profiles from different seasons show variations of ~10% or less, depending on latitude, for altitudes of 3 km and below. The largest differences are found poleward of 30°. While the daytime and nighttime mean values are, as expected, essentially indistinguishable from one another, the error envelopes differ drastically due to the influence of solar background noise during daylight measurements. In this study, we use nighttime measurements only.

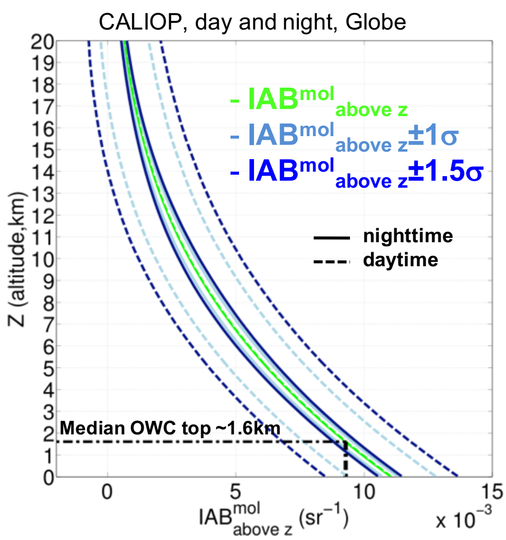

Figure B1: Nighttime (solid) and daytime (dashed) simulated vertical profile of integrated attenuated backscatter above any given altitude, z, $IAB^{mol}_{above\ z}$ (green curve). The light blue (respectively dark

Atmos. Chem. Phys. Discuss., https://doi.org/10.5194/acp-2018-1090
Manuscript under review for journal Atmos. Chem. Phys.
Discussion started: 6 November 2018

blue) envelope shows 1 (respectively 1.5) standard deviation (σ) around the $IAB^{mol}_{above\ z}$ profile. Data was generated by the CALIPSO lidar simulator [Powell et al., 2002 and 2006]. The $IAB^{mol}_{above\ z}$ value associated to the median OWC top height of ~1.6 km in our dataset corresponds to 0.0093 sr^{-1}.

In this study, we assume "clear air" when $IAB^{tot}_{aboveCloud}$ is within the simulated $IAB^{mol}_{aboveCloud}$ value ± 1σ (i.e., the light blue envelope shown in Figure B1). This definition of "clear air above" conditions is somewhat more restrictive than those imposed in previous studies. For example, Liu et al. [2015] conducted an extensive study of AAC optical depths and lidar ratios using CALIOP measurements over the tropical and southeast Atlantic. To identify clear air above cloud cases, Liu et al. [2015] require that the integrated attenuated scattering ratio, defined as

$$ASR = \frac{\int_{8km}^{OWC_{top}} (\beta_m(r)+\beta_a(r)) T_m^2(0,r) T_a^2(0,r) dr}{\int_{8km}^{OWC_{top}} \beta_m(r) T_m^2(0,r) dr} \quad \text{(B7)}$$

, fall within the range of 0.95 < ASR < 1.05, irrespective of cloud top altitude. For comparison, at the maximum OWC top altitude used in our analyses (3 km), ($IAB^{mol}_{aboveCloud}$ ± 1σ) / $IAB^{mol}_{aboveCloud}$ = 1 ± 0.0380. This restriction tightens for lower cloud top heights; e.g., at our mean OWC top altitude of 1.6 km, ($IAB^{mol}_{aboveCloud}$ ± 1σ) / $IAB^{mol}_{aboveCloud}$ = 1 ± 0.0325.

The pioneering study by Chand et al. [2008], who first used the CALIOP DR method to assess the radiative effects of aerosols above clouds, took a different approach to identifying "clear above cloud" cases. Rather than examining the overlying IAB, they instead assumed clear air above conditions

Atmos. Chem. Phys. Discuss., https://doi.org/10.5194/acp-2018-1090
Manuscript under review for journal Atmos. Chem. Phys.
Discussion started: 6 November 2018

whenever $IAB^{OWC}{}_{SS} > 0.025\ sr^{-1}$. As will be shown in section B3, in addition to the $IAB^{mol}{}_{aboveCloud}$ limits cited above, our study also enforces limits on $IAB^{OWC}{}_{SS,CAC}$. This combination of limits on both $IAB^{mol}{}_{aboveCloud}$ and $IAB^{OWC}{}_{SS,CAC}$ serves to more effectively reject aerosol-contaminated profiles from the "clear above" data set than either one alone.

B3. Process median seasonal maps of Integrated Attenuated Backscatter of Opaque Water Clouds showing Clear Air Above

Once we select specific OWCs (i.e., that satisfy the criteria of Table B2) and define which ones are "unobstructed" (see section B2), we can easily compute $IAB^{OWC}{}_{SS,CAC}$ by using Eq. (B3). For clouds that totally attenuate the lidar signal (i.e., cloud optical depths greater than ~6 [Young et al., 2018]), $IAB^{OWC}{}_{SS,CAC}$ in Eq. (2) or Eq. (B1) is related to the OWC lidar ratio (called S_c), so that

$$S_c = 1 / (2 \times \eta^{OWC} \times IAB^{OWC}{}_{CAC}) = 1 / (2 \times IAB^{OWC}{}_{SS,CAC}) \quad \text{(B8)}$$

[Platt, 1973]. OWC S_c values are relatively stable at the visible and near infrared wavelengths [Pinnick et al., 1983, O'Connor et al., 2004], but show large variations over land [Pinnick et al., 1983; Hu et al., 2006]. S_c is known to vary as a function of cloud droplet microphysics, and is especially sensitive to cloud droplet effective radius (R_e) and the imaginary part of the refractive index (see Fig. 8 of Deaconu et al. [2017]). Hu et al., [2006], Liu et al. [2015] and Deaconu et al. [2017] show that a decrease of R_e is often paired with an increase of estimated S_c at 532 nm for pure, non-aerosol-contaminated water clouds (i.e., cloud droplets having an imaginary refractive index of 0).

Atmos. Chem. Phys. Discuss., https://doi.org/10.5194/acp-2018-1090
Manuscript under review for journal Atmos. Chem. Phys.
Discussion started: 6 November 2018

As an example, Figure B3a shows the median nighttime CALIOP S_c values over the globe during 2008. Figure B3b shows MODIS AQUA-derived mean liquid water R_e in 2008 (using MODIS Level 3 monthly product "Cloud Effective Radius Liquid Mean Mean").

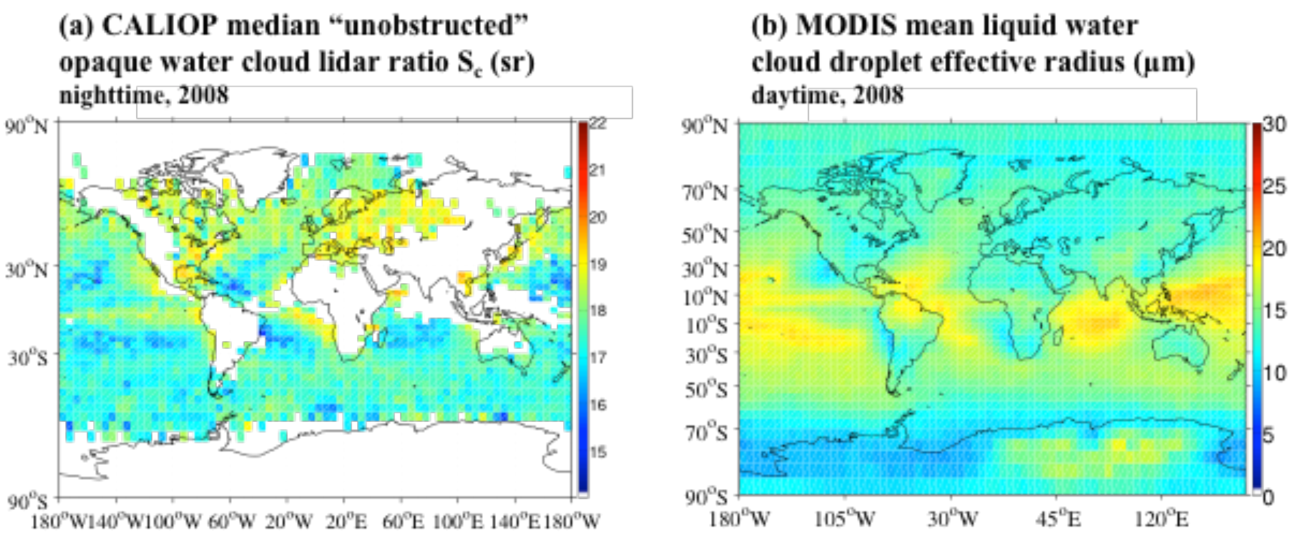

Figure B3: a) Global CALIOP yearly median nighttime "unobstructed" (i.e. clear air above) OWC lidar ratio, S_c, in 2008 that satisfy all criteria of Table B2. For the reasons outlined in this section, any OWC along the CALIOP track for which $S_c > 20$ sr or $S_c < 14$ sr is deleted before temporal and spatial averaging. White pixels show a limited number of OWCs; b) Global MODIS yearly mean daytime liquid water cloud droplet effective radius, R_e (in μm, "Cloud Effective Radius Liquid Mean Mean" parameter from MODIS MYD08_M3 product).

Atmos. Chem. Phys. Discuss., https://doi.org/10.5194/acp-2018-1090
Manuscript under review for journal Atmos. Chem. Phys.
Discussion started: 6 November 2018

Greater S_c values paired with lower cloud R_e can be seen offshore and close to the west coasts of Africa and the Americas on Figure B3. Other notable regions of low cloud R_e and high S_c on Figure B3 are above industrial regions like northern Europe, the eastern US and South East Asia. These results appear to support Twomey's analysis [Twomey, 1977; Rosenfeld and Lensky, 1998], showing an enhancement of the cloud albedo through the increase of droplet number concentration and a decrease in the droplet size driven by increased aerosol concentration. On the other hand, Figure B3a mostly exhibits low S_c values (paired with large R_e) over the inter-tropical convergence zone (ITCZ), likely associated with deep convective regimes. In addition, Figure B3a generally shows larger OWC S_c values in the northern hemisphere than in the southern hemisphere, which we attribute to differences in sources of cloud condensation nuclei. Figure B3b shows patterns that are generally similar to those in Figure B3a, but of opposite intensity. Let us note that the polarization measurements from the space-borne POLDER sensor [Deschamps et al., 1994] were also used to estimate R_e of liquid water clouds over the globe [Bréon and Colzy, 2000] and seem to be in qualitative agreement with the findings of Figure B3b.

During our assessment of 5 years of CALIOP data over the globe, we have observed significantly higher "unobstructed" OWC S_c values (i.e., S_c > 20 sr, not shown on Fig B3a) near the coasts of West Africa and over the region of SE Asia (e.g., see Young et al., [2018]). These may be physically plausible and either (1) associated with small cloud R_e, resulting from the Twomey's effect as explained above or (2) associated with the presence of light-absorbing aerosols residing within the OWCs [Mishchenko et al., 2014; Chylek and Hallett, 1992; Wittbom et al., 2014]. These aerosols would be undetected in our $IAB^{mol}_{aboveCloud}$ clear air selection method (see section B2) and would impact the chemical composition of the cloud droplets, modifying their backscattered light. The latter is well

Atmos. Chem. Phys. Discuss., https://doi.org/10.5194/acp-2018-1090
Manuscript under review for journal Atmos. Chem. Phys.
Discussion started: 6 November 2018

Atmospheric Chemistry and Physics Discussions

illustrated in Fig. 8 of Deaconu et al. [2017], which shows simulations of cloud S_c with an imaginary part of the refraction index equals to 0.0001, as a function of cloud droplet effective radius. Other reasons for these unusually high S_c values could be the sources of uncertainty noted (a), (b), (c) and (d) in the beginning of section B, with (c) (i.e., the SNR of the backscatter data within the layer) possibly having a much higher impact on S_c than all other factors. An additional source of uncertainty on the retrieval of S_c could be a failure of the CALIPSO surface detection scheme. If CALIOP fails to detect the surface adequately, part of the Earth's surface could be misclassified as an opaque water cloud and these misclassified clouds would have abnormally high S_c.

Let us note that the vast majority of the S_c values reported in the literature (i.e., in Hu et al., [2006], Liu et al. [2015] and Deaconu et al., [2017]) are estimated using a Mie code and not directly measured. However, none of these results show S_c values above 20 sr for non-aerosol-contaminated OWCs. On the other hand (and to add a lower bracket on our OWC S_c calculations), none of these results show S_c values below 14 sr. For this reason, we have imposed an additional threshold on the OWC S_c values as part of step (S3) in Table B1: we delete any "unobstructed" OWC along the CALIOP track for which $S_c > 20$ sr (i.e., unrealistically small water cloud droplets) or an $S_c < 14$ sr (i.e., unrealistically large water cloud droplets). Every OWC S_c value along the CALIOP track was then compiled to produce four global median seasonal 4°x5° maps of OWC S_c using 5 years of night-time CALIOP data (from 2008 to 2012).

Atmos. Chem. Phys. Discuss., https://doi.org/10.5194/acp-2018-1090
Manuscript under review for journal Atmos. Chem. Phys.
Discussion started: 6 November 2018

There is additional precedent for establishing an upper limit of S_c = 20 sr. Note that, from Eq. B8, the value of $IAB^{OWC}{}_{SS,CAC}$ corresponding to S_c = 20 sr is 0.025 sr^{-1}. As mentioned earlier, this is the same OWC IAB threshold value used by Chand et al. [2008] to identify their "clear air above" cases.

B4. Extinction-to-Backscatter (Lidar) Ratio

Table B3 lists some typical, recently reported values of the aerosol lidar ratios (S_a) measured for various aerosol types. These data include CALIOP retrievals for several species (e.g., marine, dust, and smoke) as well as ground-based measurements made using high spectral resolution lidars (HSRL) and Raman lidars.

Table B3: retrieved aerosol extinction-to-backscatter ratios (S_a) reported in the literature (PBL: Planetary Boundary Layer)

S_a (532 nm, sr)	Aerosol type, S_a value and references (non-exhaustive)
20-25	**Marine** PBL North Atlantic and PBL tropical Indian ocean 23 sr [Müller et al., 2007]
26-30	**Marine** global ocean 26 sr [Dawson et al., 2014]; Mix of **Marine** and **Pollution**, case study offshore East Coast USA 26.3 sr [Josset et al., 2011]
31-35	**Gobi dust** Beijing PBL 35 sr [Müller et al., 2007]; Mix of **Marine and dust**, two case studies Caribbean, 32-33 sr [Josset et al., 2011]

Atmos. Chem. Phys. Discuss., https://doi.org/10.5194/acp-2018-1090
Manuscript under review for journal Atmos. Chem. Phys.
Discussion started: 6 November 2018

36-40	**Arabian dust** 33.7 ± 6.7 to 39.1 ± 5.1 sr [Mamouri et al., 2013] **Sahara dust** 39.8 ± 1.4 sr [Omar et al., 2010]
41-45	**Urban** South Africa 41±13sr [Giannakaki et al., 2016] **Desert dust** Middle East 42.6 sr and India 43.8 sr [Schuster et al., 2012]; **Desert dust** Tropical North Atlantic 45.1±8.8 sr [Liu et al., 2015]
46-50	**Desert dust** African Sahel 49.7sr [Schuster et al., 2012]
51-55	**Desert dust** PBL 55 sr [Müller et al., 2007]; **Urban** Haze central Europe 53 sr [Müller et al., 2007]; **Asian dust** 51 sr [Liu et al., 2002]
56-60	**Desert dust** non-Sahel North Africa 55.4 sr [Schuster et al., 2012]; **Desert dust** Africa 60 sr [Pedrós et al., 2010]
66-70	**Biomass burning** South East Atlantic 70.8±16.2 sr [Liu et al., 2015]
71-85	**Biomass burning** South Africa 75±14sr [Giannakaki et al., 2016]

Atmos. Chem. Phys. Discuss., https://doi.org/10.5194/acp-2018-1090
Manuscript under review for journal Atmos. Chem. Phys.
Discussion started: 6 November 2018

Atmospheric Chemistry and Physics Discussions

Data Availability:

This study used the following A-Train data products: (i) CALIPSO version 3 lidar level 1 profile products (Powell et al. [2013]; NASA Langley Research Center Atmospheric Science Data Center; https://doi.org/10.5067/CALIOP/CALIPSO/CAL_LID_L1-ValStage1-V3-01_L1B-003.01; last access: 26 September 2018), (ii) CALIPSO version 3 lidar level 2 5 km cloud layer products (Powell et al. [2013]; NASA Langley Research Center Atmospheric Science Data Center; https://doi.org/10.5067/CALIOP/CALIPSO/CAL_LID_L2_05kmCLay-Prov-V3-01_L2-003.01; last access: 26 September 2018), (iii) MODIS Atmosphere L2 Version 6 Aerosol Product (Levy and Hsu [2015]; NASA MODIS Adaptive Processing System, Goddard Space Flight Center, USA; http://dx.doi.org/10.5067/MODIS/MOD04_L2.006; last access: 26 September 2018), and (iv) L2 Version 3 OMI products OMAERO [Stein-Zweers and Veefkind, 2012] and OMAERUV [Torres, 2006].

Author contributions:

The overarching research goals were formulated by Dr Redemann. Dr. Kacenelenbogen, Dr. Young and Mr. Vaughan influenced the evolution of these research goals. Dr. Kacenelenbogen carried out the formal analyses, investigations and visualizations and wrote the original draft. All co-authors have reviewed and edited the multiple drafts of the manuscript. The methodology behind the global application of the DR method to CALIOP measurements was first developed by Dr. Hu, and adapted by Dr. Kacenelenbogen, Dr. Young, Mr. Vaughan, and Ms. Powell to accommodate the requirements of this study. The methodology for using this combination of A-Train satellites to infer aerosol intensive radiative properties was conceptualized by Dr Redemann. The joint MODIS-OMI-CALIOP aerosol radiative properties were developed and provided by Dr. Shinozuka, Mr. Livingston and Ms. Zhang. Dr. LeBlanc performed the radiative transfer calculations that provided Direct Aerosol Radiative Effects estimates in clear skies and above clouds.

Competing interests:

The authors declare that they have no conflict of interest.

Acknowledgements:

We thank the CALIPSO lidar science working group and data management team for their efforts in providing and discussing these data sets. We appreciate the comments of the reviewers that have helped us to improve the paper. We are grateful for comments from Dr. Zuidema and Dr. Wood on cloud microphysics over the South East Atlantic. This study was funded in part by NASA's Research Opportunities in Space and Earth Sciences (ROSES) program under grant NNH12ZDA001N-CCST.

References

Alfaro-Contreras, R., Zhang, J., Reid, J. S., Campbell, J. R., and Holz, R. E., Evaluating the impact of aerosol particles above cloud on cloud optical depth retrievals from MODIS, J. Geophys. Res. Atmos., 119, 5410–5423, doi:10.1002/2013JD021270, 2014.

Alfaro-Contreras, R., Zhang, J., Campbell, J. R., and Reid, J. S., Investigating the frequency and interannual variability in global above-cloud aerosol characteristics with CALIOP and OMI, Atmos. Chem. Phys., 16, 47-69, doi:10.5194/acp-16-47-2016, 2016.

Anderson, G., Clough, S., Kneizys, F., Chetwynd, J., and Shettle, E., AFGL atmospheric constituent profiles (0-120 km), Tech. Rep. AFGL-TR-86-0110, Air Force Geophys. Lab., Hanscom Air Force Base, Bedford, Mass, 1986.

Anderson, T. E., Charlson, R. J., Winker, D. M., Ogren, J. A., and Holmen, K.: Mesoscale Variations of Tropospheric Aerosols, J. Atmos. Sci., 60, 119–136, 2003.

Arola, A., et al., Influence of observed diurnal cycles of aerosol optical depth on aerosol direct radiative effect, Atmos. Chem. Phys., 13.15: 7895-7901., 2013.

Blot, R., and Coauthors, Ultrafine sea spray aerosol over the southeastern Pacific: Open-ocean contributions to marine boundary layer CCN. Atmos. Chem. Phys., 13, 7263–7278, doi:10.5194/acp-13-7263-2013, 2013.

Bréon, F. M. and S. Colzy, Global distribution of cloud droplet effective radius from POLDER polarization measurements, Geo. Reas. Lett., Vol. 27, N 24, P 4065-4068, 2000.

Bréon, F-M., Aerosol extinction-to-backscatter ratio derived from passive satellite measurements, Atmos. Chem. Phys. 13.17: 8947-8954, 2013.

Buras, R., Dowling, T., and Emde, C., New secondary-scattering correction in DISORT with increased efficiency for forward scattering, J. Quant. Spectrosc. Ra., 112, 2028–2034, 2011.

Candlish, L. M., R. L. Raddatz, G. G. Gunn, M. G. Asplin and D. G. Barber: A Validation of CloudSat and CALIPSO's Temperature, Humidity, Cloud Detection, and Cloud Base Height over the Arctic Marine Cryosphere, Atmos. Ocean, 51, 249–264, doi:10.1080/07055900.2013.798582, 2013.

Chand, D., T. L. Anderson, R. Wood, R. J. Charlson, Y. Hu, Z. Liu, and M. Vaughan, Quantifying above-cloud aerosol using spaceborne lidar for improved understanding of cloudy-sky direct climate forcing, J. Geophys. Res., 113, D13206, doi:10.1029/007JD009433, 2008.

Chand, D., R. Wood, T. L. Anderson, S. K. Satheesh, and R. J. Charlson, Satellite-derived direct radiative effect of aerosols dependent on cloud cover, Nat. Geosci., 2, 181–184, doi:10.1038/ngeo437, 2009.

Chand, D., Hegg, D. A., Wood, R., Shaw, G. E., Wallace, D., and Covert, D. S., Source attribution of climatically important aerosol properties measured at Paposo (Chile) during VOCALS, Atmos. Chem. Phys., 10, 10789–10801, doi:10.5194/acp-10-10789-2010, 2010.

Chang, Ian, and Sundar A. Christopher, "Identifying Absorbing Aerosols Above Clouds From the Spinning Enhanced Visible and Infrared Imager Coupled With NASA A-Train Multiple Sensors." IEEE. T. Geosci. Remote. S., 54.6: 3163-3173, 2016.

Chang, Ian, and Sundar A. Christopher., "The impact of seasonalities on direct radiative effects and radiative heating rates of absorbing aerosols above clouds." Q. J. Roy. Meteor. Soc., 143.704: 1395-1405, 2017.

Chung, C. E., V. Ramanathan, D. Kim, and I. A. Podgorny: Global anthropogenic aerosol direct forcing derived from satellite and ground-based observations. J. Geophys. Res., 110, D24207, doi:10.1029/2005JD006356, 2005.

Chylek, Petr, and John Hallett, "Enhanced absorption of solar radiation by cloud droplets containing soot particles in their surface." Q. J. Roy. Meteor. Soc., 118.503: 167-172, 1992.

Costantino, L. and Bréon, F.-M., Satellite-based estimate of aerosol direct radiative effect over the South-East Atlantic, Atmos. Chem. Phys. Discuss., 13, 23295-23324, doi:10.5194/acpd-13-23295-2013, 2013.

Cox, Charles, and Walter Munk. "Measurement of the roughness of the sea surface from photographs of the sun's glitter." Josa 44.11: 838-850, 1954.

Dawson, N. Meskhidze, D. Josset, and S. Gassó**,** A new study of sea spray optical properties from multi-sensor spaceborne observations, Atmos. Chem. Phys. Discuss., 14, 213–244, 2014.

Deaconu, L. T., F. Waquet, D. Josset, N. Ferlay, F. Peers, F. Thieuleux, F. Ducos, N. Pascal, D. Tanré, and P. Goloub, "Consistency of aerosols above clouds characterization from A-Train active and passive measurements", Atmos. Meas. Tech. Discuss., doi:10.5194/amt-2017-42, 2017.

De Graaf, M., L. G. Tilstra, P. Wang, and P. Stammes, Retrieval of the aerosol direct radiative effect over clouds from spaceborne spectrometry, J. Geophys. Res., 117, D07207, doi:10.1029/2011JD017160, 2012.

De Graaf, M., N. Bellouin, L. G. Tilstra, J. Haywood, and P. Stammes, Aerosol direct radiative effect of smoke over clouds over the southeast Atlantic Ocean from 2006 to 2009, Geophys. Res. Lett., 41, 7723–7730, doi:10.1002/2014GL061103, 2014.

Deschamps, P. Y., F. M. Breon, M. Leroy, A. Podaire, A. Bricaud, J. C. Buriez and G. Seze, The POLDER mission: Instrument characteristics and scientific objectives. IEEE T. Geosci. Remote. S., 32, 598-615, 1994.

Devasthale, A., and M. A. Thomas, A global survey of aerosol-liquid water cloud overlap based on four years of CALIPSO–CALIOP data, Atmos. Chem. Phys., 11, 1143–1154, 2011.

Di Girolamo L, Liang L, Platnick S. A global view of one-dimensional solar radiative transfer through oceanic water clouds. Geophys. Res. Lett.;37:L18809, 2010.

Emde, C., Buras-schnell, R., Kylling, A., Mayer, B., Gasteiger, J., Hamann, U., Kylling, J., Richter, B., Pause, C., Dowling, T. and Bugliaro, L., The libRadtran software package for radiative transfer calculations (version 2.0.1), Geosci. Model Dev., 9, 1647–1672, doi:10.5194/gmd-9-1647-2016, 2016.

Feng, N., and S. A. Christopher, Measurement-based estimates of direct radiative effects of absorbing aerosols above clouds, J. Geophys. Res. Atmos., 120, 6908–6921, doi:10.1002/ 2015JD023252, 2015.

Fernald F.G., B. M. Herman and J. A. Reagan, Determination of Aerosol Height Distribution by Lidar, J. Appl. Meteor., 11, 482-489, 1972.

Fu, Q. and Liou, K., On the correlated k-distribution method for radiative transfer in nonhomogeneous atmospheres, J. Atmos. Sci., 49, 2139–2156, 1992.

Giannakaki, E., van Zyl, P. G., Müller, D., Balis, D., and Komppula, M.: Optical and microphysical characterization of aerosol layers over South Africa by means of multi-wavelength depolarization and Raman lidar measurements, Atmos. Chem. Phys., 16, 8109-8123, https://doi.org/10.5194/acp-16-8109-2016, 2016.

Haywood, J. M., S. R. Osborne, P. Francis, M. Glew, N. Loeb, E. Highwood, D. Tanré, G. Myhre, P. Formenti, and E. Hirst, Radiative properties and direct radiative effect of Saharan dust measured by the C-130 aircraft during SHADE: 1. Solar spectrum, J. Geophys. Res., 108(D18), 8577, doi:10.1029/2002JD002687, 2003.

Herman, J. R., P. K. Bhartia, O. Torres, C. Hsu, C. Seftor, and E. Celarier, Global distribution of UV-absorbing aerosols from Nimbus 7/TOMS data, J. Geophys. Res., 102, 16,911–16,922, 1997.

Holben, B. N., Eck, T. F., Slutsker, I., Tanr´e, D., Buis, J. P., Setzer, A., Vermote, E., Reagan, J. A., Kaufman, Y. J., Nakajima, T., Lavenu, F., Jankowiak, I., and Smirnov, A., AERONET–A federated instrument network and data archive for aerosol characterization, Remote Sens. Environ., 66, 1–16, 1998.

Hu, Y., Vaughan, M., Winker, D., Liu, Z., Noel, V., Bissonnette, L., Roy, G., McGill, M., and Trepte, C., A simple multiple scattering-depolarization relation of water clouds and its potential applications, Proceedings of 23nd International Laser Radar Conference, Nara, Japan, 24–28 July, 19–22, 2006.

Hu, Y., Vaughan, M., Liu, Z., Lin, B., Yang, P., Flittner, D., Hunt, W., Kuehn, R., Huang, J., Wu, D., Rodier, S., Powell, K., Trepte, C., and Winker, D.: The depolarization-attenuated backscatter relation: CALIPSO lidar measurements vs. theory, Optics Express, 15, 5327–5332, doi:10.1364/OE.15.005327, 2007a.

Hu, Y, M. Vaughan, Z. Liu, K. Powell, and S. Rodier, Retrieving Optical Depths and Lidar Ratios for Transparent Layers Above Opaque Water Clouds From CALIPSO Lidar Measurements, IEEE Geosci. Remote Sens. Lett., 4, 523-526, 2007b.

Hu, Y., et al., CALIPSO/CALIOP cloud phase discrimination algorithm, J. Atmos. Ocean. Tech., 26.11: 2293-2309, 2009.

Hunt, W. H., D. M. Winker, M. A. Vaughan, K. A. Powell, P. L. Lucker, and C. Weimer, CALIPSO lidar description and performance assessment, J. Atmos. Ocean. Tech., 26, 1214–1228, doi:10.1175/2009JTECHA1223.1, 2009.

Jethva, H., O. Torres, L. A. Remer, and P. K. Bhartia, A color ratio method for simultaneous retrieval of aerosol and cloud optical hickness of above-cloud absorbing aerosols from passive sensors: Application to MODIS measurements, IEEE T. Geosci. Remote. S., 51(7), 3862–3870, doi:10.1109/TGRS.2012.2230008, 2013.

Jethva, H., O. Torres, F. Waquet, D. Chand, and Y. Hu, How do A-train sensors intercompare in the retrieval of abovecloud aerosol optical depth? A case study-based assessment, Geophys. Res. Lett., 41, doi:10.1002/2013GL058405, 2014.

Josset D., R Rogers, J Pelon, Yongxiang Hu, Zhaoyan Liu, Ali Omar, and Peng-Wang Zhai, CALIPSO lidar ratio retrieval over the ocean, Vol. 19, No. 19 / Opt. Express., 2011.

Kacenelenbogen, M., J. Redemann, M. A. Vaughan, A. H. Omar, P. B. Russell, S. Burton, R. R. Rogers, R. A. Ferrare, and C. A. Hostetler, An evaluation of CALIOP/CALIPSO's aerosol-above-cloud detection and retrieval capability over North America, J. Geophys. Res. Atmos., 119, 230–244, doi:10.1002/2013JD020178, 2014.

Kassianov, E., et al. "Do diurnal aerosol changes affect daily average radiative forcing?." Geophys. Res. Lett., 40.12: 3265-3269, 2013.

Kim, S.-W., E.-S. Chung, S.-C. Yoon, B.-J. Sohn, and N. Sugimoto, "Intercomparisons of cloud-top and cloud-base heights from ground-based Lidar, CloudSat and CALIPSO measurements", Int. J. Remote Sens., 32, 1179–1197, doi:10.1080/01431160903527439, 2011.

Kim, M.-H., A. H. Omar, M. A. Vaughan, D. M. Winker, C. R. Trepte, Y. Hu, Z. Liu and S.-W. Kim, 2017: "Quantifying the low bias of CALIPSO's column aerosol optical depth due to undetected aerosol layers", *J. Geophys. Res. Atmos.*, **122**, 1098–1113, doi:10.1002/2016JD025797.

King, Michael D., et al. "Spatial and temporal distribution of clouds observed by MODIS onboard the Terra and Aqua satellites." IEEE T. Geosci. Remote. S., 51.7: 3826-3852, 2013.

Klein, S. A. and Hartmann, D. L., The seasonal cycle of low stratiform clouds, J. Climate, 6, 1587–1606, 1993.

Atmos. Chem. Phys. Discuss., https://doi.org/10.5194/acp-2018-1090
Manuscript under review for journal Atmos. Chem. Phys.
Discussion started: 6 November 2018

Kovacs, T.: Comparing MODIS and AERONET aerosol optical depth at varying separation distances to assess ground-based validation strategies for spaceborne lidar, J. Geophys. Res., 111, D24203, doi:10.1029/2006JD007349, 2006.

Leahy, L. V., R. Wood, R. J. Charlson, C. A. Hostetler, R. R. Rogers, M. A. Vaughan, and D. M. Winker, On the nature and extent of optically thin marine low clouds, J. Geophys. Res., 117, D22201, doi:10.1029/2012JD017929, 2012.

Levy, R., and C. Hsu. "MODIS Atmosphere L2 Aerosol Product." *NASA MODIS Adaptive Processing System*, 2015.

Liu, Z., N. Sugimoto, and T. Murayama, Extinction-to-backscatter ratio of Asian dust observed with high-spectral-resolution lidar and Raman lidar, Appl. Optics., 41.15, 2760-2767, 2002.

Liu, D., Wang, Z., Liu, Z., Winker, D. M., and Trepte, C., A height resolved global view of dust aerosols from the first year CALIPSO lidar measurements, J. Geophys. Res., 113, D16214, doi:10.1029/2007JD009776, 2008.

Liu, Z., R. Kuehn, M. Vaughan, D. Winker, A. Omar, K. Powell, C. Trepte, Y. Hu, and C. Hostetler, The CALIPSO cloud and aerosol discrimination: Version 3, Algorithm and test results, 25th International Laser and radar conference, 2010.

Liu Z, D. Winker, A. Omar, M. Vaughan, J. Kar, C. Trepte, Y. Hu, and G. Schuster, Evaluation of CALIOP 532nm aerosol optical depth over opaque water clouds, Atmos. Chem. Phys., 15, 1265–1288, 2015.

Mamouri, R. E., et al. Low Arabian dust extinction-to-backscatter ratio. Geophys. Res. Lett., 40.17:

Atmos. Chem. Phys. Discuss., https://doi.org/10.5194/acp-2018-1090
Manuscript under review for journal Atmos. Chem. Phys.
Discussion started: 6 November 2018

4762-4766, 2013.

Matus, Alexander V., et al., The role of clouds in modulating global aerosol direct radiative effects in spaceborne active observations and the Community Earth System Model." J. Climate, 28.8: 2986-3003, 2015.

McGill, M. J., M. A. Vaughan, C. R. Trepte, W. D. Hart, D. L. Hlavka, D. M. Winker, and R. Kuehn, Airborne validation of spatial properties measured by the CALIPSO lidar, J. Geophys. Res., **112**, D20201, doi:10.1029/2007JD008768, 2007.

Meyer, K., S. Platnick, L. Oreopoulos, and D. Lee, Estimating the direct radiative effect of absorbing aerosols overlying marine boundary layer clouds in the southeast Atlantic using MODIS and CALIOP, J. Geophys. Res. Atmos., 118, 4801–4815, doi:10.1002/jgrd.50449, 2013.

Meyer, K., S. Platnick, and Z. Zhang: Simultaneously inferring above-cloud absorbing aerosol optical thickness and underlying liquid phase cloud optical and microphysical properties using MODIS, J. Geophys. Res. Atmos., 120, 5524–5547, doi:10.1002/2015JD023128, 2015.

Min, M., and Z. Zhang, On the influence of cloud fraction diurnal cycle and sub-grid cloud optical thickness variability on all-sky direct aerosol radiative forcing, J. Quant. Spectrosc. RA., 142: 25-36, 2014.

Mishchenko, Michael I., et al., Optics of water cloud droplets mixed with black-carbon aerosols, Opt. Lett., 39.9: 2607-2610, 2014.

Mitchell R. M., S. K. Campbell, and Y. Qin, Recent increase in aerosol loading over the Australian

Atmos. Chem. Phys. Discuss., https://doi.org/10.5194/acp-2018-1090
Manuscript under review for journal Atmos. Chem. Phys.
Discussion started: 6 November 2018

arid zone, Atmos. Chem. Phys., 10, 1689– 1699, 2010.

Müller, D., A. Ansmann, I. Mattis, M. Tesche, U. Wandinger, D. Althausen, and G. Pisani, Aerosol-type-dependent lidar ratios observed with Raman lidar, J. Geophys. Res., 112, D16202, doi:10.1029/2006JD008292, 2007.

Noel, V., Chepfer, H., Hoareau, C., Reverdy, M., and Cesana, G.: Effects of solar activity on noise in CALIOP profiles above the South Atlantic Anomaly, Atmos. Meas. Tech., 7, 1597–1603, doi:10.5194/amt-7-1597-2014, 2014.

O'Connor, E. J., A. J. Illingworth, and R. J. Hogan, A technique for autocalibration of cloud lidar, J. Atmos. Ocean. Tech., 21, 777– 786, doi:10.1175/1520-0426, 2004.

Oikawa, E., T. Nakajima, T. Inoue, and D. Winker, A study of the shortwave direct aerosol forcing using ESSP/CALIPSO observation and GCM simulation, J. Geophys. Res. Atmos., 118, 3687–3708, doi:10.1002/jgrd.50227, 2013.

Omar, A., et al., The CALIPSO automated aerosol classification and lidar ratio selection algorithm, J. Atmos. Ocean. Tech., 26, 1994–2014, doi:10.1175/2009JTECHA1231.1, 2009.

Omar, A., et al., Extinction-to-backscatter ratios of Saharan dust layers derived from in situ measurements and CALIPSO overflights during NAMMA, J. Geophys. Res., 115, D24217, doi:10.1029/2010JD014223, 2010.

Oreopoulos, Lazaros, Robert F. Cahalan, and Steven Platnick. "The plane-parallel albedo bias of liquid clouds from MODIS observations." *Journal of Climate* 20.20: 5114-5125, 2007.

Pedrós R., V. Estellés, M. Sicard, J. L. Gómez-Amo, M. Pilar Utrillas, J. A. Martínez-Lozano, F. Rocadenbosch, C. Pérez, and J. M. Baldasano Recio, Climatology of the Aerosol Extinction-to-Backscatter Ratio from Sun-Photometric Measurements, IEEE T. Geosci. Remote. S., 48- 1, 2010.

Peers F., F. Waquet, C. Cornet, P. Dubuisson, F. Ducos, P. Goloub, F. Szczap, D. Tanré, and F. Thieuleux, Absorption of aerosols above clouds from POLDER/PARASOL measurements and estimation of their direct radiative effect, Atmos. Chem. Phys., 15, 4179–4196, 2015.

Peng et al., The cloud albedo-cloud droplet effective radius relationship for clean and polluted clouds from RACE and FIRE.ACE, J. Geophys. Res., VOL. 107, NO. D11, 10.1029/2000JD000281, 2002.

Penner, J. E., Soot and smoke aerosol may not warm climate. J. Geophys. Res., 108, 4657, doi:10.1029/2003JD003409, 2003.

Peters, K., J. Quaas, and N. Bellouin, Effects of absorbing aerosols in cloudy skies: A satellite study over the Atlantic Ocean. Atmos. Chem. Phys., 11, 1393–1404, doi:10.5194/acp-11-1393-2011, 2011.

Pinnick, R. G., Jennings, S. G., Chylek, P., Ham, C., and Grandy Jr., W. T., Backscatter and extinction in water clouds, J. Geophys. Res., 88, 6787–6796, 1983.

Platnick, S., et al., MODIS Atmosphere L3 Monthly Product. NASA MODIS Adaptive Processing System, Goddard Space Flight Center, USA, doi:10.5067/MODIS/MOD08_M3.006, 2015.

Platt, C. M. R., Lidar and radiometric observations of cirrus clouds, J. Atmos. Sci., 30.6: 1191-1204, 1973.

Powell, K., W. Hunt, and D. Winker, Simulations of CALIPSO Lidar Data, Proceedings of the 21st International Laser Radar Conference (ILRC), Quebec City, Quebec (available at http://www-calipso.larc.nasa.gov/resources/pdfs/ILRC_2002/ILRC2002_Powell_Simulator.pdf), 2002.

Powell, K. A., Development of the CALIPSO Lidar Simulator", M.S. Thesis, Department of Applied Science, The College of William and Mary, 228 pp, 2005.

Powell, K. A., Liu, Z., and W. H. Hunt, Simulation of Random Electron Multiplication in CALIPSO Lidar Photomultipliers, Proceedings of the 23rd International Laser Radar Conference (ILRC), Nara, Japan (available at http://www-calipso.larc.nasa.gov/resources/pdfs/ILRC_2006/Powell-PhotomultiplierSimulation-2P-23.pdf), 2006.

Powell, K. A., et al., CALIPSO lidar calibration algorithms. Part I: Nighttime 532-nm parallel channel and 532-nm perpendicular channel, J. Atmos. Ocean. Tech., 26.10: 2015-2033, 2009.

Powell, K., Vaughan, M., Winker, D., Lee, K.-P.. Pitts, M., Trepte, C., Detweiler, P., Hunt, W., Lambeth, J., Lucker, P., Murray, T., Hagolle, O., Lifermann, A., Faivre, M., Garnier, A., and Pelon, J.: Cloud–Aerosol LIDAR Infrared Pathfinder Satellite Observations (CALIPSO) Data Products Catalog, Document No: PC-SCI-503, Release 3.5, available on-line at https://www-calipso.larc.nasa.gov/products/CALIPSO_DPC_Rev3x5.pdf (last access: 12 October 2018), 2013.

Quijano, A. L., I. N. Sokolik, and O. B. Toon, Radiative heating rates and direct radiative forcing by mineral dust in cloudy atmospheric conditions. J. Geophys. Res., 105, 12 207–12 219, doi:10.1029/2000JD900047, 2000.

Atmos. Chem. Phys. Discuss., https://doi.org/10.5194/acp-2018-1090
Manuscript under review for journal Atmos. Chem. Phys.
Discussion started: 6 November 2018

Redemann, J., Vaughan, M. A., Zhang, Q., Shinozuka, Y., Russell, P. B., Livingston, J. M., Kacenelenbogen, M., and Remer, L. A., The comparison of MODIS-Aqua (C5) and CALIOP (V2 & V3) aerosol optical depth, Atmos. Chem. Phys., 12, 3025-3043, doi:10.5194/acp-12-3025-2012, 2012.

Redemann J., Y. Shinozuka, M. Kacenelenbogen, S. LeBlanc, M. Segal-Rozenhaimer, M. Vaughan, P. Stier, N. Schutgens, Use of A-Train aerosol observations to constrain direct aerosol radiative effects (DARE) and comparisons with AeroCom phase II DARE results, in preparation.

Remer, L. A., Y. J. Kaufman, D. Tanré, S. Mattoo, D. A. Chu, J. V. Martins, R.-R. Li, C. Ichoku, R. C. Levy, R. G. Kleidman, T. F. Eck, E. Vermote and B. N. Holben, The MODIS aerosol algorithm, products and validation. J. Atmos. Sci.,62 (4),947-973, 2005.

Rogers, R. R., Hostetler, C. A., Hair, J. W., Ferrare, R. A., Liu, Z., Obland, M. D., Harper, D. B., Cook, A. L., Powell, K. A., Vaughan, M. A., and Winker, D. M., Assessment of the CALIPSO Lidar 532 nm attenuated backscatter calibration using the NASA LaRC airborne High Spectral Resolution Lidar, Atmos. Chem. Phys., 11, 1295-1311, doi:10.5194/acp-11-1295-2011, 2011.

Rosen, J., S. Young, J. Laby, N. Kjome, and J. Gras, Springtime aerosol layers in the free troposphere over Australia: Mildura Aerosol Tropospheric Experiment (MATE 98), J. Geophys. Res., 105(D14), 17833–17842, *doi:10.1029/2000JD900208,* 2000.

Rosenfeld, D. and Lensky, I. M., Satellite-based insights into precipitation formation processes in continental and maritime convective clouds, B. Am. Meteorol. Soc., 79, 2457–2476, 1998.

Russell P. B. R., T. J. Swissler, and McCormick M. P., Methodology for error analysis and

Atmos. Chem. Phys. Discuss., https://doi.org/10.5194/acp-2018-1090
Manuscript under review for journal Atmos. Chem. Phys.
Discussion started: 6 November 2018

simulation of lidar aerosol measurements, Appl. Optics., Vol. 18, Issue 22, pp. 3783-3797, 1979.

Santese, M., De Tomasi, F., and Perrone, M. R.: AERONET versus MODIS aerosol parameters at different spatial resolutions over southeast Italy, J. Geophys. Res., 112, D10214, doi:10.1029/2006JD007742, 2007.

Sayer, Andrew M., et al., Extending "Deep Blue" aerosol retrieval coverage to cases of absorbing aerosols above clouds: Sensitivity analysis and first case studies, J. Geophys. Res. Atmos., 121.9: 4830-4854, 2016.

Schulz, M., Textor, C., Kinne, S., Balkanski, Y., Bauer, S., Berntsen, T., Berglen, T., Boucher, O., Dentener, F., Guibert, S., Isaksen, I. S. A., Iversen, T., Koch, D., Kirkevåg, A., Liu, X., Montanaro, V., Myhre, G., Penner, J. E., Pitari, G., Reddy, S., Seland, Ø., Stier, P., and Takemura, T., Radiative forcing by aerosols as derived from the AeroCom present-day and pre-industrial simulations, Atmos. Chem. Phys., 6, 5225-5246, doi:10.5194/acp-6-5225-2006, 2006.

Schuster, Gregory L., et al. "Comparison of CALIPSO aerosol optical depth retrievals to AERONET measurements, and a climatology for the lidar ratio of dust." *Atmos. Chem. Phys* 12.16: 7431-7452, 2012.

Schutgens, N. A. J., Nakata, M., and Nakajima, T.: Validation and empirical correction of MODIS AOT and AE over ocean, Atmos. Meas. Tech., 6, 2455–2475, doi:10.5194/amt-6-2455-2013, 2013.

Shinozuka, Y. and Redemann, J.: Horizontal variability of aerosol optical depth observed during the ARCTAS airborne experiment, Atmos. Chem. Phys., 11, 8489–8495, doi:10.5194/acp-11-8489-2011, 2011.

Atmos. Chem. Phys. Discuss., https://doi.org/10.5194/acp-2018-1090
Manuscript under review for journal Atmos. Chem. Phys.
Discussion started: 6 November 2018

Stamnes, K., Tsay, S.-C., Wiscombe, W., and Jayaweera, K., Numerically stable algorithm for discrete–ordinate–method radiative transfer in multiple scattering and emitting layered media, Appl. Opt., 27, 2502–2509, 1988.

Stein-Zweers D. and P. Veefkind, OMI/Aura Multi-wavelength Aerosol Optical Depth and Single Scattering Albedo 1-orbit L2 Swath 13x24 km V003, NASA Goddard Space Flight Center, Goddard Earth Sciences Data and Information Services Center (GES DISC), 10.5067/Aura/OMI/DATA2001 <https://doi.org/10.5067/Aura/OMI/DATA2001>, 2012.

Thorsen, T. J., Q. Fu, and J. M. Comstock, Comparison of the CALIPSO satellite and ground-based observations of cirrus clouds at the ARM TWP sites, J. Geophys. Res., **116**, D21203, doi:10.1029/2011JD015970, 2011.

Thorsen, T. J., and Fu, Q.: CALIPSO-inferred aerosol direct radiative effects: bias estimates using ground-based Raman lidars, J. Geophys. Res. Atmos., 120, 12,209–12,220, doi:10.1002/2015JD024095, 2015.

Thorsen, T. J., R. A. Ferrare, C. A. Hostetler, M. A. Vaughan, and Q. Fu, The impact of lidar detection sensitivity on assessing aerosol direct radiative effects, Geophys. Res. Lett., **44**, 9059–9067, doi:10.1002/2017GL074521, 2017.

Torres O., OMI/Aura Near UV Aerosol Optical Depth and Single Scattering Albedo 1-orbit L2 Swath 13x24 km V003, Greenbelt, MD, USA, Goddard Earth Sciences Data and Information Services Center (GES DISC), 10.5067/Aura/OMI/DATA2004 <https://doi.org/10.5067/Aura/OMI/DATA2004>, 2006.

Torres, O., J. Hiren, and P. K. Bhartia, Retrieval of aerosol optical depth above clouds from OMI

Atmos. Chem. Phys. Discuss., https://doi.org/10.5194/acp-2018-1090
Manuscript under review for journal Atmos. Chem. Phys.
Discussion started: 6 November 2018

observations: Sensitivity analysis and case studies. J. Atmos. Sci., 69, 1037–1053, 2012.

Toth, T. D., J. R. Campbell, J. S. Reid, J. L. Tackett, M. A. Vaughan, J. Zhang, and J. W. Marquis, 2018: Minimum Aerosol Layer Detection Sensitivities and their Subsequent Impacts on Aerosol Optical Thickness Retrievals in CALIPSO Level 2 Data Products, *Atmos. Meas. Tech.*, **11**, 499–514, doi:10.5194/amt-11-499-2018.

Twomey, S., Influence of pollution on shortwave albedo of clouds, J. Atmos. Sci., 34(7), p1149–1152, doi:10.1175/1520-0469(1977) 034<1149:TIOPOT>2.0.CO;2, 1977.

Várnai, T. and A. Marshak, MODIS observations of enhanced clear sky reflectance near clouds, Geophys. Res. Lett., 36, L06807, doi:10.1029/2008GL037089, 2009.

Vaughan, M.,K. Powell, R.Kuehn, S. Young, D. Winker, C.Hostetler, W.Hunt, Z. Liu, M. McGill, and B. Getzewich, Fully automated detection of cloud and aerosol layers in the CALIPSO lidar measurements, J. Atmos. Ocean. Tech., 26, 2034–2050, oi:10.1175/2009JTECHA1228.1, 2009.

Vaughan, M. A., Z. Liu, M. J. McGill, Y. Hu, and M. D. Obland, On the spectral dependence of backscatter from cirrus clouds: Assessing CALIOP's 1064 nm calibration assumptions using cloud physics lidar measurements, J. Geophys. Res., 115, D14206, doi:10.1029/2009JD013086, 2010.

Waquet F., J. Riedi, L. C. Labonnote, P. Goloub, B. Cairns, J-L. Deuzé, and D. Tanré, Aerosol Remote Sensing over Clouds Using A-Train Observations. J. Atmos. Sci., **66**, 2468–2480, 2009.

Waquet, F., F. Peers, F. Ducos, P. Goloub, S. Platnick, J. Riedi, D. Tanré, and F. Thieuleux, Global analysis of aerosol properties above clouds, Geophys. Res. Lett., 40, 5809–5814, doi:10.1002/2013GL057482, 2013a.

Atmos. Chem. Phys. Discuss., https://doi.org/10.5194/acp-2018-1090
Manuscript under review for journal Atmos. Chem. Phys.
Discussion started: 6 November 2018

Waquet, F., et al., Retrieval of aerosol microphysical and optical properties above liquid clouds from POLDER/PARASOL polarization measurements, Atmos. Meas. Tech., 6, 991–1016, doi:10.5194/amt-6-991, 2013b.

Watson-Parris, D., Schutgens, N., Winker, D., Burton, S. P., Ferrare, R. A., and Stier, P.: On the limits of CALIOP for constraining modelled free-tropospheric aerosol, *Geophys. Res. Lett.*, **45**, 9260–9266, doi:10.1029/2018GL078195, 2018.

Wen, G., A. Marshak, R. F. Cahalan, L. A. Remer, and R. G. Kleidman, 3-D aerosol–cloud radiative interaction observed in collocated MODIS and ASTERg images of cumulus cloud fields, J. Geophys. Res., 112, D13204, doi:10.1029/2006JD008267, 2007.

Wilcox, E. M., Direct and semi-direct radiative forcing of smoke aerosols over clouds, Atmos. Chem. Phys., 12, 139-149, doi:10.5194/acp-12-139-2012, 2012.

Winker, D. M., M. A. Vaughan, A. Omar, Y. Hu, K. A. Powell, Z. Liu, W. H. Hunt, and S. A. Young, Overview of the CALIPSO mission and CALIOP data processing algorithms, J. Atmos. Ocean. Tech., 26, 2310–2323, doi:10.1175/2009JTECHA1281.1, 2009.

Wittbom, C., Eriksson, A. C., Rissler, J., Carlsson, J. E., Roldin, P., Nordin, E. Z., Nilsson, P. T., Swietlicki, E., Pagels, J. H., and Svenningsson, B., Cloud droplet activity changes of soot aerosol upon smog chamber ageing, Atmos. Chem. Phys., 14, 9831-9854, doi:10.5194/acp-14-9831-2014, 2014.

Xu, Hui, et al. "On the influence of the diurnal variations of aerosol content to estimate direct aerosol radiative forcing using MODIS data." Atmos. Environ., 141: 186-196, 2016.

Yorks, J., D. Hlavka, M. Vaughan, M. McGill, W. Hart, S. Rodier, and R. Kuehn, Airborne Validation of Cirrus Cloud Properties Derived from CALIPSO Lidar Measurements: Spatial Properties, J. Geophys. Res., **116**, D19207, doi:10.1029/2011JD015942, 2011.

Young, S. A., and M. A. Vaughan, The retrieval of profiles of particulate extinction from Cloud Aerosol Lidar Infrared Pathfinder Satellite Observations (CALIPSO) data: Algorithm description, J. Atmos. Ocean. Tech., 26, 1105–1119, doi:10.1175/2008JTECHA1221.1, 2009.

Young, S. A., Vaughan, M. A., Garnier, A., Tackett, J. L., Lambeth, J. B., and Powell, K. A.: Extinction and Optical Depth Retrievals for CALIPSO's Version 4 Data Release, Atmos. Meas. Tech. Discuss., doi:10.5194/amt-2018-182, accepted for publication, 2018.

Young, S. A., Vaughan, M. A., Garnier, A., Tackett, J. L., Lambeth, J. B., and Powell, K. A.: Extinction and Optical Depth Retrievals for CALIPSO's Version-4 Data Release: Supplementary Material, doi:10.5194/TBD, 2018.

Yu, H., et al. "A review of measurement-based assessments of the aerosol direct radiative effect and forcing." *Atmospheric Chemistry and Physics* 6.3: 613-666, 2006.

Yu, H., Y. Zhang, M. Chin, Z. Liu, A. Omar, L. A. Remer, Y. Yang, T. Yuan, and J. Zhang, An integrated analysis of aerosol above clouds from A-Train multi-sensor measurements, Remote Sens. Environ., 121: 125–131, 2012.

Yu, H., and Z. Zhang, New directions: Emerging satellite observations of above-cloud aerosols and direct radiative forcing, Atmos. Environ., 72, 36–40, doi:10.1016/j.atmosenv.2013.02.017, 2013.

Atmos. Chem. Phys. Discuss., https://doi.org/10.5194/acp-2018-1090
Manuscript under review for journal Atmos. Chem. Phys.
Discussion started: 6 November 2018

Zelinka, M. D., Klein, S. A., and Hartmann, D. L., Computing and Partitioning Cloud Feedbacks Using Cloud Property Histograms. Part I: Cloud Radiative Kernels. J. Climate, 833 25:3715–3735, 2012.

Zhang, J., J. S. Reid, and B. N. Holben, An analysis of potential cloud artifacts in MODIS over ocean aerosol optical thickness products, Geophys. Res. Lett., 32, L15803, doi: 10.1029/2005GL023254, 2005.

Zhang Z, Platnick S. An assessment of differences between cloud effective particle radius retrievals for marine water clouds from three MODIS spectral bands. J. Geophys. Res.,; 116:D20215, 2011.

Zhang Z, Ackerman AS, Feingold G, Platnick S, Pincus R, Xue H. Effects of cloud horizontal inhomogeneity and drizzle on remote sensing of cloud droplet effective radius: case studies based on large-eddy simulations. J. Geophys. Res.; 117:D19208, 2012.

Zhang, Z., K. Meyer, S. Platnick, L. Oreopoulos, D. Lee, and H. Yu, A novel method for estimating shortwave direct radiative effect of above-cloud aerosols using CALIOP and MODIS data, Atmos. Meas. Tech., 7(6), 1777–1789, doi:10.5194/amt-7-1777-2014, 2014.

Zhang, Z., Meyer, K., Yu, H., Platnick, S., Colarco, P., Liu, Z., Oreopoulos, L., Shortwave direct radiative effects of above-cloud aerosols over global oceans derived from 8 years of CALIOP and MODIS observations, Atmos. Chem. Phys., 16.5: 2877-2900, 2016.